Second Harmonic Generation Spectroscopy of the Potential Induced Surface Reconstruction of the Au (110) Electrode in Perchloric Acid Electrolyte.

Erika Revesz

Thesis submitted to the
School of Graduate Studies and Research
University of Ottawa
in partial fulfillment of the requirements for the
M.Sc.degree in the
Ottawa-Carleton Chemistry Institute

ISBN 0-612-15755-5

UNIVERSITÉ D'OTTAWA
UNIVERSITY OF OTTAWA

I dedicate this thesis to my ***Mother*** *who could not pursue her own studies because of the war, but did everything in her power to help her children become educated.*

Acknowledgments

I would like to express my gratitude to my supervisor, Dr. Mario Morin for allowing me to work on this project and directing me with patience during this research.

I am grateful to Sylvie Morin for her help with single crystal electrochemistry and x-ray diffraction at the beginning of my research.

I would like to express my appreciation to my colleagues Dr. Dale Keefe, Dr. Arthur Vardanyan, Dr. Dongfang Yong for their help during this project.

I thank Jeannine Bordeleau for her help with the library service.

Finally, I give thanks to my friend Dr. Robert Chlebek for his support during this research.

Abstract

In-situ optical second harmonic generation (SHG) spectroscopy was used to examine the potential induced surface reconstruction of a Au (110) surface in a solution of 0.01 M $HClO_4$. The SHG rotational anisotropy was measured at different potentials using the fundamental beam (1064 nm) of the Nd:YAG laser. Analysis of the data shows that the overall symmetry of the surface is C_S. It was also found that the second order nonlinear susceptibility for both the reconstructed and the unreconstructed surface have a large three fold symmetry component. We suggest that the three-fold symmetry source is partly due to the (111) microfacets that are present on the (110) surface.

List of figures

Table of Contents

Chapter 3: Experimental

Chapter 4: Result and Discussion

Chapter 1: Introduction

1.1. Introduction

The purpose of this experiment is to investigate the process of reconstruction on the Au (110) electrode surface in a weakly adsorbed electrolyte using non-linear spectroscopy [1]. This chapter presents an introduction as well as a short explanation of the low index faces of gold, the electrochemistry of single crystal gold electrodes related to SHG and surface reconstruction.

Experimental methods for structural characterization of the electrode/electrolyte interface can be divided into two broad categories: *ex-situ* methods; where the electrode is removed from solution and probed in ultra high vacuum with various spectroscopies, *in-situ* methods; where the electrode surface is examined under electrochemical conditions.

Ex-situ structural methods are the various electron spectroscopies, e.g. low energy electron diffraction (LEED) [2] or x-ray photoelectron spectroscopy (XPS) [3]. The main limitation of these methods is that the electrode has to be removed from solution and characterized in ultra-high vacuum (UHV). This makes it difficult to determine how the structure of the electrode surface in UHV is related to the surface prior to removal from solution. Such an approach can lead to false conclusions about the structure of the electrode in solution.

In-situ methods are more appropriate to study metal-solution interfaces because these methods characterize the surface in the electrolyte solution. However, the requirements are more stringent to be able to distinguish between the response of the species detected at the surface from the same species distributed in the bulk of the solution. The X-ray methods, such as the extended x-ray adsorption fine structure (EXAFS) [4], the grazing incidence x-ray scattering (GIXS) [5] and surface x-ray scattering (SXS) [6,7] can give information about the interface. In-situ structural techniques such as the scanning tunneling microscopy (STM) have emerged only recently. STM allows a direct access to the real-space atomic structure of metal surfaces in electrochemical as well as in ultrahigh vacuum environment [8-10]. The possible difficulty with the STM method is that the probing tip can cause stray capacitance in solution which may interfere with the observation. To minimize this interference the probing tip is covered usually with a glass coating or "nail polish" but this may introduce contamination [11].

Recently, optical laser techniques, such as SHG have been applied to study the structural changes occuring at the metal-electrolyte interface. SHG is well suited to study surfaces of centrosymmetric media (e.g., fcc metals) because the nonlinear optical response mainly arises at the surface were the inversion symmetry is broken. Several electrode materials were studied; Ag [12,13], Au [14], Pt [15]. This technique can also be applied to probe molecular adsorption on a metal surfaces, both in UHV and at the metal-liquid interface [16-18].

SHG can probe structural changes and phase transitions of adsorbate overlayers less than a monolayer coverage. SHG can also be used to monitor surface reactions and surface dynamics on metals [16].

1.2 Low index faces of gold

One of the reason for studying single crystal surfaces has to do with the high level of their symmetry. The ordered structure of the single crystal surface permits the study of the relationship between structure and chemical reactivity.

The atomic structural arrangement is characteristic of each single-crystal surface. The faces of single crystals are identified in terms of Miller indices. In this notation the orientation of the face is given relative to the crystal axes. In Figure 1.1 (A) an example of the reference coordinate system for the (111) plane is shown where the three lattice points, each one unit from the origin defines the crystallographic (111) plane. In Figure 1.1 (B) the Miller indices of some important planes of the cubic close packed system are shown [19]. To calculate Miller indices (hkl), first the intercepts of the plane on the three crystal axes have to be found, then their reciprocals are taken and the three smallest integers are reduced to have the same ratio [20-22]. A low index means that the Miller indices are either one or zero. As an example, the (100) is a low index face and the (332) plane is a high index face. SHG studies on some of the low index faces of gold can be found in references [23,24].

A

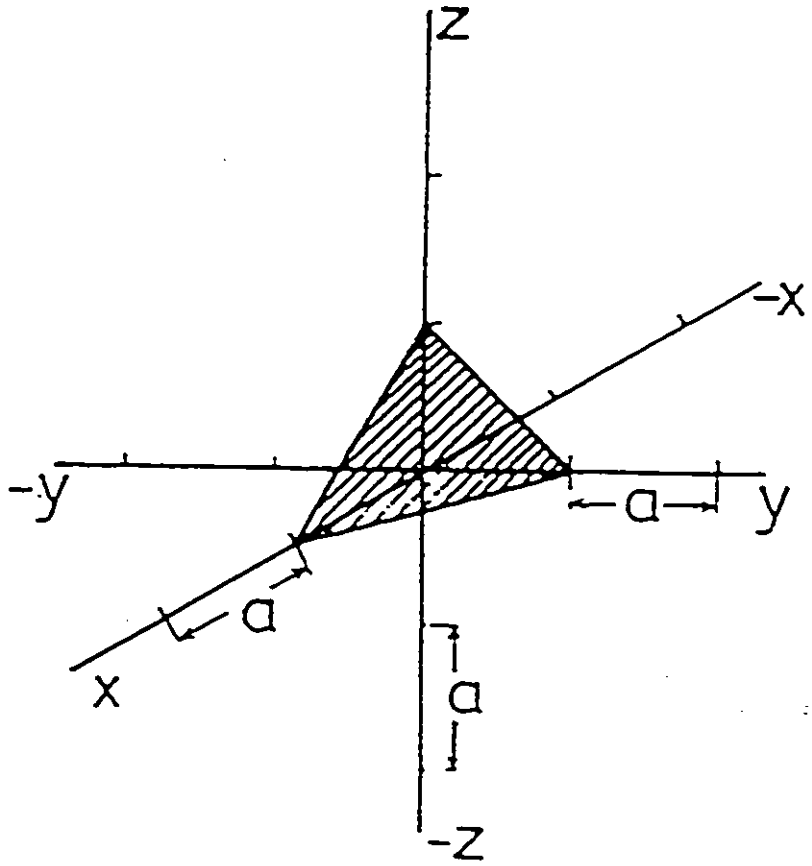

B

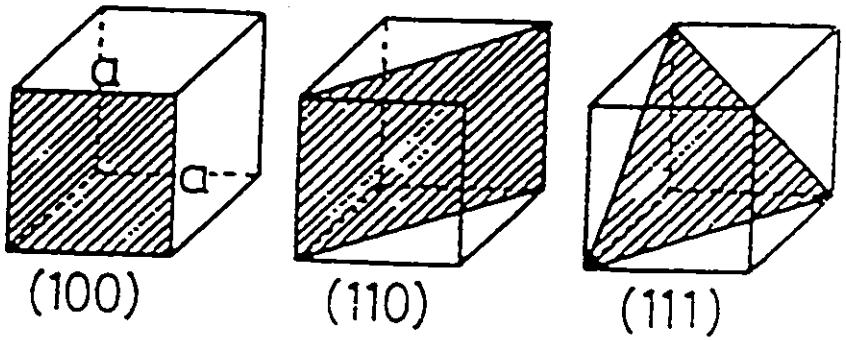

Figure 1.1. (A) The reference system to determine the Miller indices.

(B) the important low index planes of gold are illustrated. Taken from reference [22].

1.3. Electrochemistry related to the surface reconstruction of gold

In this section the electrical double layer and the potential of zero charge are discussed. The electrochemistry of the double layer region for the electrode/electrolyte interface gives information on the surface reconstruction.

The *potential of zero charge* (pzc) is defined as the potential at where the net charge of the electrode is zero in a given electrochemical system. At more positive potentials the electrode has an excess positive surface charge, and at more negative potentials, the electrode has an excess negative charge. The pzc is characteristic of the electrode material and depends to some degree on the components of the electrolyte solution. In the case of no adsorption the pzc is linearly related to the *electronic work function* (the energy required to remove an electron from the highest occupied level of the solid) of the metal surface [25]. For metals with higher melting points, such as Ag, Cu, Au the pzc is dependent on crystallographic orientation [19]. The pzc for Au (110) is about -40 mV vs the saturated calomel electrode (SCE), for the more densely packed Au (111) it is about +300 mV (SCE) in 0.01 M $HClO_4$ electrolyte. Qualitatively a more positive pzc corresponds to a more densely packed surface because it has the highest electronic work function. A more negative pzc corresponds to a rougher, less densely packed surface because it has the lowest work function. If there is an adsorption on the electrode surface and if the charge of the adsorbate is positive the pzc shifts positively.

This shift increases as the concentration of the adsorbate increases. If the charge of the adsorbate is negative the pzc shifts negatively with the increasing concentration.

The pzc can be measured with different methods such as the radiotracer method, friction, differential capacitance or electrocapillarity [25,26]. For single crystals, the pzc is usually measured with *differential capacitance* as shown in Figure 1.2 (b). The capacitance of the metal-electrolyte interface characterizes its ability to store charge when the potential is disturbed. The change in charge density with the variation of potential can be expressed with the equation,

$$C_d = (\frac{\partial \sigma}{\partial V}) \qquad (1.1)$$

The differential capacitance is the slope of the surface charge σ *vs.* the potential V in equation (1.1). The capacitance measurement is taken in the absence of specific adsorption and surface reconstruction where the electrolyte is at a sufficiently low concentration. An approximate method can be used to determine the pzc. This involves expanding the double layer of the CV as shown in Figure 1.2 (a). The pzc is taken as the potential at which the current is the smallest.

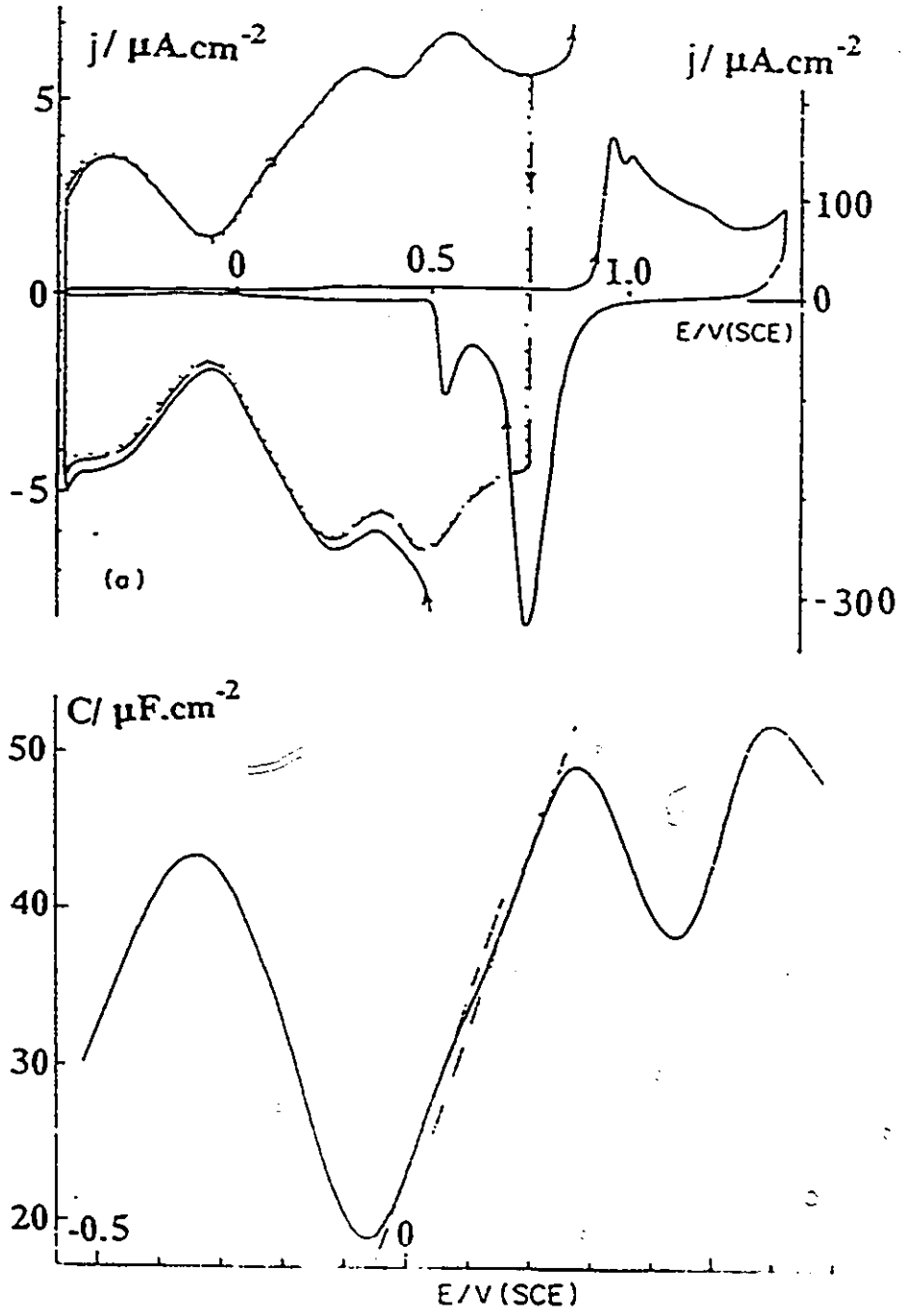

Figure 1.2. (a) Literature Cyclic Voltammogram of Au (110) in 0.01 M $HClO_4$. 80 mV/s; 23 ± 1 C°. (B) The corresponding C(E) curves in the same solution, 5mV/s. (Taken from Reference [28].)

i. The electrical double layer

The electrode-solution interface behaves like a capacitor. The metal solution interface is called the *electrical double layer.* The rates of the various electrode processes can be affected by the structure of the double layer. In electricity a capacitor is a device for storing electric charge. It usually consists of two parallel conducting sheets separated by some dielectric material. The behavior of the capacitor is governed by the equation

$$\frac{q}{V} = C \qquad (1.2)$$

where q is the charge (in Coulombs, C), V is the potential across the interface (in Volts, V), and C is the capacitance (in Farads, F). When potential is applied across a capacitor, charge accumulates on the metal sheets according to equation 1.2. During this process a charging current will flow. One plate of the capacitor contains a surplus of electrons and the other is deficient of electrons. The electrode-solution interface behaves similarly, one plate is the electrode and the other is the solution. There is charging on the electrode and charging of the solution at the surface, and whether the charge is negative or positive is depends on the applied potential across the interface. If there is charge on the metal this means an excess or deficiency of electrons on its surface relative to the charge at the pzc. On the other hand a charge on the solution represents excess of either cations or anions close to the electrode surface.

The electrical double layer consists of the metal electrode and the solution [27]. The solution side can be devided into several regions as illustrated on Figure 1.3. A layer next to the electrode surface is called the *inner layer*, which contains solvent molecules and some other species *adsorbed* to the surface. The total charge density in this inner layer is σ^i , which is from the specifically adsorbed ions. The next layer, at a distance x_2 called the *outer Helmholtz plane* (OHP) which is located from the electrical center of the specifically adsorbed ions to the electrical center of the solvated ions. The interaction is longe-range electrostatic between the charged metal and the solvated ions because of the bigger distance among them. The solvated ions are *nonspecifically adsorbed* and randomly distributed in the *diffuse layer*. The diffuse layer extends from OHP to the bulk of the electrolyte solution.

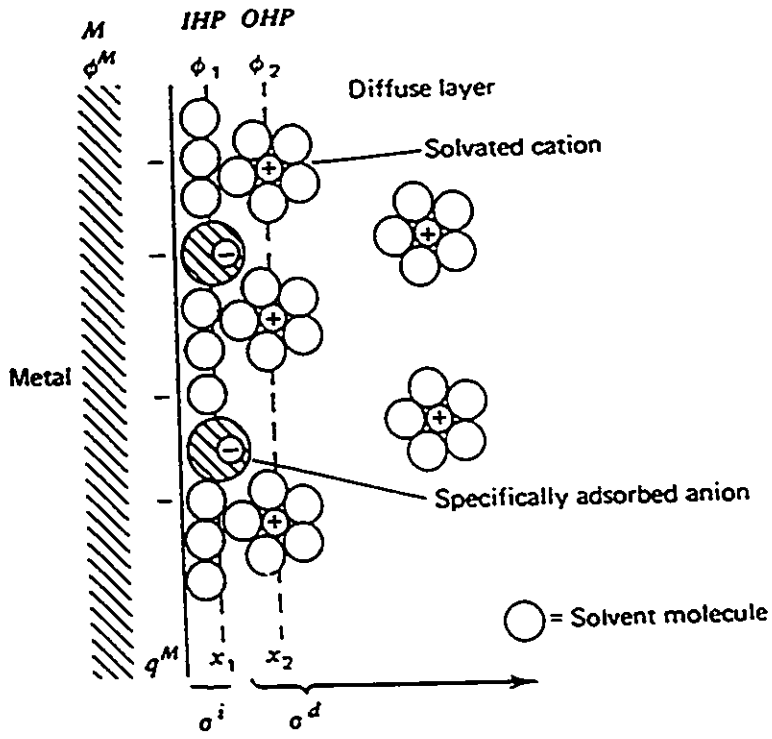

Figure 1.3. The model of the electrical double layer

Taken from reference [27].

ii. Cyclic voltammetry of Au (110)

The cyclic voltammetry (CV) of gold polycrystal and also single crystal faces are used to characterize the interface and have been studied extensively [28]. A typical CV for Au (110) is shown in Figure 1.2 (a) [28]. This figure represents the CV for Au (110) at 80 mV/s in 0.01 M $HClO_4$. The *double layer region* is located between -0.5 to 0.7 V (SCE) and it is symmetric. As the potential is cycled in the positive direction a monolayer of surface oxide is formed between 1.0 and 1.4 V (SCE). This oxide layer is completely reduced as the potential is cycled in the reverse direction around 0.9 V (SCE). The process of oxide formation is reversible, this means that all of the monolayer of oxide that is formed in the anodic cycle is reduced in the cathodic cycle. The position and the shape of the peak potentials are characteristic of each gold single crystal face for a given electrolyte solution. We have assigned the different peaks related to the formation of the reversible surface oxide following a mechanism proposed previously [29]. For Au (110) in 0.01 M $HClO_4$ in the positive going anodic cycle a small current peak in the CV marked as OA1 corresponds to the first charge transfer in the two electron transfer process where a monolayer of the OH species is deposited on the surface between the specifically adsorbed ClO_4^- anions (Figure 1.4).

$$[Au_x\, ClO_4^-]Au + H_2O \Leftrightarrow [Au_x\, ClO_4^-]AuOH + H^+ + e \qquad (1.3)$$

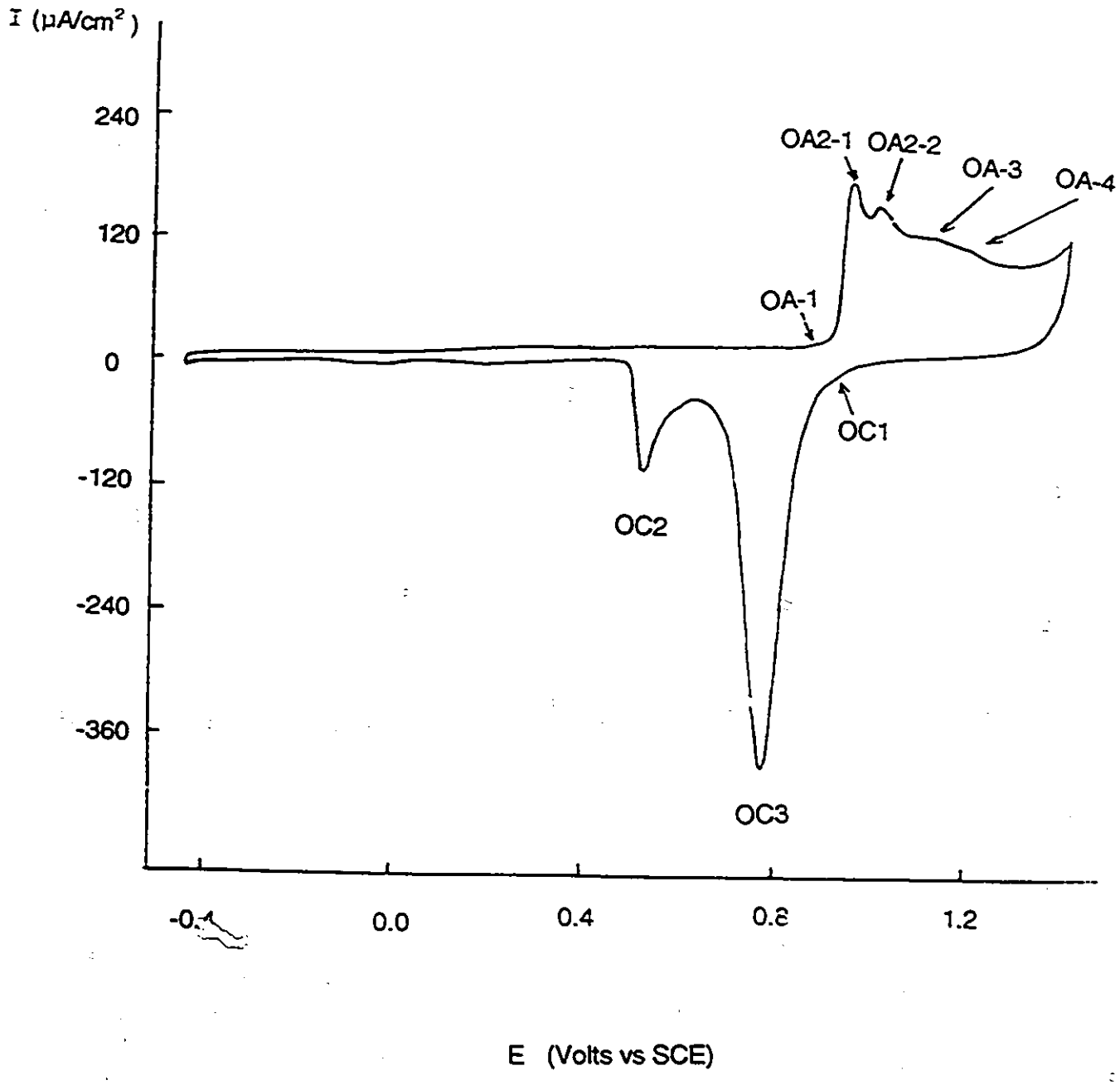

Figure 1.4. Cyclic voltammetry of Au (110) in 0.01 M $HClO_4$. Scan rate 80 mV/s. 23 ±1 °C.

The second very sharp peak and a smaller peak next to it, OA2-1 and OA2-2 at 0.96 V and 1.0 V (SCE) correspond to OH deposition that replace the ClO_4^- anions.

$$Au_x ClO_4^- + H_2O \rightarrow Au_{x-1} + AuOH + ClO_4^- + H^+ + e \qquad (1.4)$$

When the coverage of OH is high enough a turnover process can occur as shown in equation (1.5).

$$\begin{matrix} OH & OH \\ | & | \\ Au & Au \end{matrix} \longrightarrow \begin{matrix} Au & OH \\ | & | \\ OH & Au \end{matrix} \qquad (1.5)$$

According to Conway et al. [29] the anion replacement and the turnover process (RTO) occurs simultaneously.

The relatively small anodic peak, OA3 relates to the completion of the OH monolayer as represented by the following process

$$[AuOH]_{x-1} Au + H_2O \rightarrow xAuOH + H^+ + e \qquad (1.6)$$

The last feature in the anodic cycle before the potential scan is reversed is the peak OA4 which corresponds to the second charge transfer process.

$$AuOH \rightarrow AuO + H^{+} + e \qquad (1.7)$$

In eqn. (1.7) other oxidation species, like $Au(OH)_2$ can be formed. These equations above, do not represent stoichiometric quantities, they only show the possible surface interactions. On the reverse or cathodic cycle the reduction of the oxide monolayer occurs. Peak OC1 is the counterpart of OA1 where the deposited OH is being reduced. The large peak OC3 represents a two step reduction process of the RTO sequence where the first step is the reduction of the turnover process.

$$OHAu \rightarrow AuOH \qquad (1.8\ a)$$

The second step the actual electrochemical reduction process is

$$AuOH + H^{+} + e \rightarrow Au + H_2O \qquad (1.8\ b)$$

The OC2 peak represents the reduction of the deposited OH species in the OA2 process.

1.4. Electrode surface reconstruction

To understand surface processes, such as adsorption or chemical reactions on surfaces, a detailed model of the surface atomic geometry is essential [30]. Furthermore, the electrocatalytic activity of a metal surface can be influenced by its crystallographic orientation.

The origin of reconstruction and relaxation of a solid surface is coming from the tendency towards a minimum surface free energy. The simplest surface model assumes that, the periodicity and the spacing of the outermost layers of the surface atoms are identical to the bulk of the solid. On a real surface this arrangement of atoms often does not represent the most stable structure, because the electronic configuration and the coordination of the atoms on the surface are not the same as in the bulk due to surface reconstruction and relaxation.

The surface structural changes can be divided into two types [30-33]:

i. *Relaxation*: When a surface relaxes the topmost layer retains the symmetry of the bulk, but the atomic distances vertical to the surface are different from the bulk. In some cases specially surfaces with low symmetry a given layer can also shift laterally against the layers in the bulk. The surface relaxation involves small atomic displacements. In many cases there is a contraction between the first and the second layers and expansion between the second and third layers on the surface.

ii. *Surface Reconstruction*: This is a stronger surface disturbance than surface relaxation. A surface reconstruction consists of a rearrangement of the topmost layers into a different unit cell. This results in a different symmetry compared to the bulk. The surface atoms can undergo substantial lateral displacement.

Both, relaxation and reconstruction are multilayer phenomena. The reconstructive rearrangements are favored on fcc metals, like Au (110). The relaxation processes are favored on bcc metals. The reduction in surface free energy more than compensates for the increase in surface area caused by the reconstruction.

In electrochemistry the surface reconstruction can be caused by different processes: it can be spontaneous, as in vacuum [2]; or induced by the applied potential, as in Au (110) [22 (b), 34]; or caused by adsorption of molecules or atoms [23]. These types of surface restructuring, like surface roughening, the creation of steps, and faceting can cause macroscopic changes in the surface topology. These changes have an impact on the physical and chemical properties on surfaces. To examine these structural changes is especially important in electrochemistry because of their effects on the chemical reactivity.

It is known that under ultrahigh vacuum the clean surfaces of Pt, Au and Ir undergo reconstruction [11]. For example, the hexagonal close-packed (hcp) structure of the Au (100) reconstructed surface has a structural misfit between the top layer and the layers under it which causes the surface to be slightly buckled. The surface density of the reconstructed hcp surface contains about 20 % more atoms than the unreconstructed (1x1) surface. This gives a rather complicated (5x20) structure where

the Au (100) exhibits a hexagonal reconstruction where there are almost six surface atoms for every five bulk atoms along the <110> direction (Figure 1.6 (a)). The Au (111) reconstructed surface has a hexagonal dense packed structure which consists of a 4 % contraction of the surface layer in one of the three <110> directions. This causes every 23rd surface atom to be in register with the underlying bulk. This leads to the (1x23) structure (see Figure 1.6 (c). The reconstruction of the Au (110) is discussed below.

1.5. Reconstruction of Au (110) electrode in 0.01 M $HClO_4$

The Au (110) unreconstructed surface has a square unit cell structure which is shown in Figure 1.5.

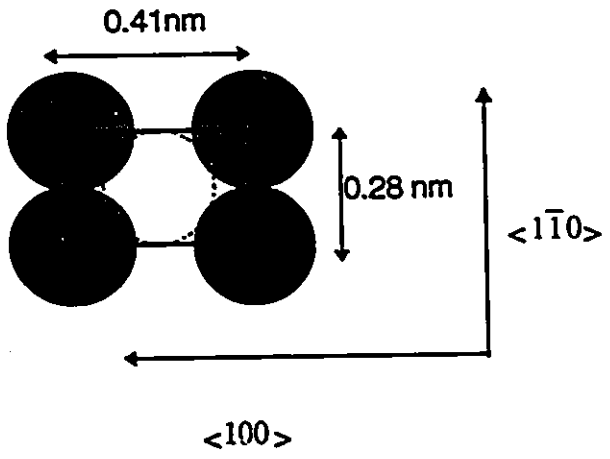

Figure 1.5. The unit cell structure of the unreconstructed Au (110) surface.

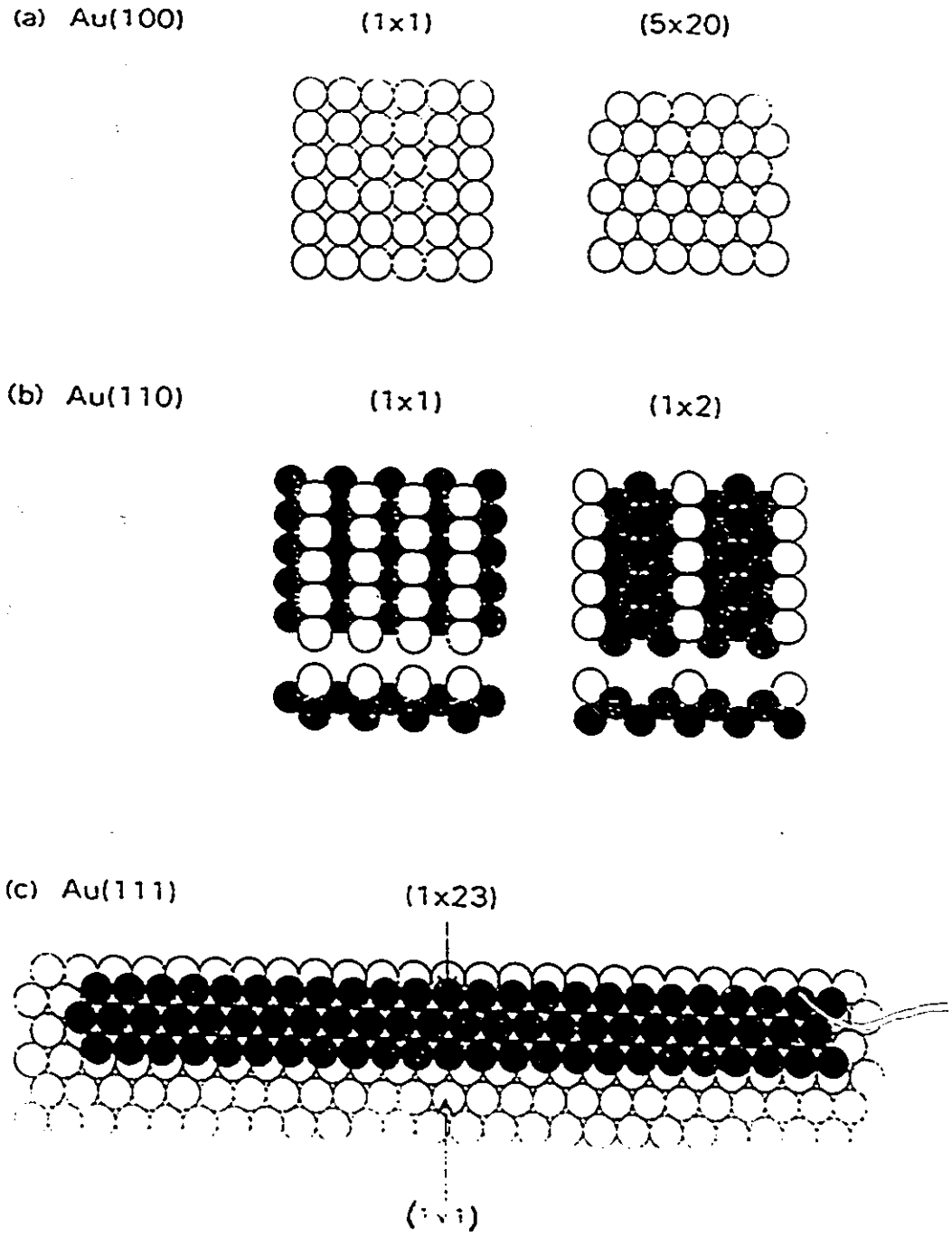

Figure 1.6. Top view of surface reconstruction of the low index faces of gold. (A) Au (100), (B) Au (110), (C) Au (111).

The surface reconstruction of Au (110) is different from those of the Au (111) and the Au (100). The Au (110) surface reconstructs spontaneously in UHV [35,36]. It forms a (1x2) also known as "missing row" type reconstruction where every second row in the <100> direction is removed (Fig.1.5 (b)) as shown by ex-situ low energy electron diffraction (LEED). This type of reconstruction leads to the formation of the (111) microfacets in the <100> direction. Similarly, another type, the (1x3) reconstruction is formed when two rows, the second and third are missing in the <100> direction. This has been confirmed by various techniques, such as electron diffraction, surface x-ray scattering and scanning tunneling microscopy [2,6,8-10]. The results of the above studies are discussed in more details below.

The suggestion of a potential induced surface reconstruction in a salt solution was based on differential capacitance measurement. The observed hysteresis between the positive and negative going sweeps, and the different values of pzc possibly arise from a change in the superficial structure of the Au (110) surface with the imposed potential [22 (b)].

The ex-situ LEED studies in UHV showed that on clean Au (110) surface the (1x2) reconstruction was stable up to +0.9 V (SCE) in 0.01 M $HClO_4$ [37]. It was beleived that the reconstruction was stable over the entire double layer region and it was not affected by the specifically adsorbed perchlorate or hydroxyl ions. However, recent in-situ STM, SXS and SHG have shown that the surface is not reconstructed

extensively at a potential positive to the pzc as was suggested from the capacitance measurements.

The in-situ surface X-ray scattering study [38] stated that at a negative potential, a poorly correlated structure which is an intermediate between the (1x2) and (1x3) structures is formed in 0.1 M $HClO_4$. In a salt solution, such as NaCl a more ordered (1x3) reconstruction seems to exists.

The in-situ scanning tunneling microscopy (STM) study showed that in 0.1 M $HClO_4$ at positive charge densities the unreconstructed (1x1) structure exists, while at a negative potential, e.g., at -0.3 V (SCE), mainly the reconstructed (1x2) and (1x3) structures exists. In salt solution, like KI, at a negative charge density, e.g., at -0.7 V (SCE) only the (1x3) reconstruction exists [8,9,10,39].

An electron diffraction study by Moritz et al. in ultrahigh vacuum [2,35,36] states that the Au (110)-(1x2) surface results in a modification of the missing row model with substantial distortions which are at least three layers deep.The spacing of the top layer is contracted by about 20%, the bond length are reduced due to the compensation by the lateral deviation in the second layer and the buckling in the third layer. The topmost rows of atoms is attracted to the second layer and the nearest neighbor in the third layer. The bond length are reduced by about 3-5 %. An analogous contraction of bond length occurs between the second and third layer at those rows of atoms where the top row is missing, consequently causing the buckling in the third layer. Taking the center of mass in the third layer as the reference point, both the second and third layer spacings are expanded slightly by about 2 %.

Part (A) of Figure 1.7. shows the side view of atomic arrangement of the unreconstructed Au (110)-(1x1) surface structure. Part (B) shows the structure of the (1x2) reconstruction, where every second row in the <100> direction is missing. Part (C) shows the (1x3) where two rows out of three are missing. In perchloric acid a mixture of the (1x2) and (1x3) reconstruction exist [2].

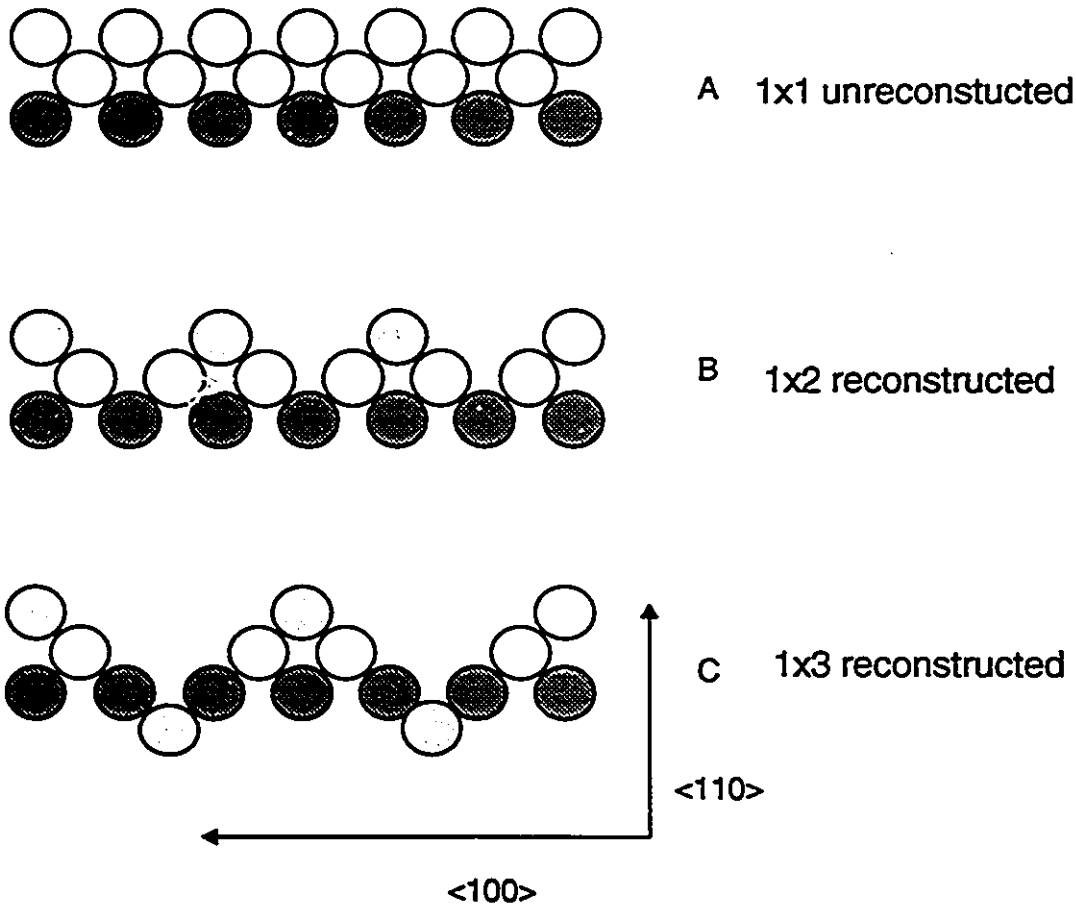

Figure 1.7. The side view of the Au (110) unreconstructed (1x1) and reconstructed (1x2) and (1x3) surface structure

Chapter 2: Theory of Surface Second Harmonic Generation

2.1. Introduction

Second harmonic generation is a nonlinear optical spectroscopy technique that can be used to probe the structure of surfaces and interfaces in a real environment. In this chapter the theory of SHG is discussed.

Most of the optical effects are linear effects, such as reflection, refraction, scattering and absorption of light. It is to say when light interacts with a material, the response is proportional to the intensity of light. These linear optical responses of matter modifies the intensity of light but they do not alter their frequencies.

Second harmonic generation, a nonlinear response, was first observed in 1961 by Franken et al. [40] when they focused the 694.3 nm ruby laser output onto a quartz crystal. They found that the transmitted light consisted two frequency components with wavelength at 694.3 and 347.15 nm. The crystal generated a second beam at exactly twice the frequency of the fundamental laser beam.

The development of lasers are linked to the development of *nonlinear optics*. Applications of nonlinear optics include the frequency doubling of a monochromatic wave (*second harmonic generation*), the utilization of two monochromatic waves to amplify a third wave (*parametric amplification*), the addition of a feedback to a parametric amplifier to create an oscillator (*parametric oscillation*), and the mixing of two monochromatic waves to generate a third wave whose frequency is the sum or the

difference of the original wave (*frequency conversion*). Nonlinear optical effects are weak and usually appear in the presence of intense electric and magnetic fields [41].

To understand the nature of the interaction one can imagine the forces felt by a single atom in an oscillating electric field. When the electric field is zero, the motion of the electrons and the nucleus in the atom are in a balanced state. When the electromagnetic field strength increases this balanced state will be disturbed, the electron distribution is distorted according to the direction of the electromagnetic field. Maxwell's theory [42] states that any accelerating (vibrating) electric charge reradiates electromagnetic energy. As a result of this, every vibrating atom becomes a secondary source of electromagnetic radiation with the same frequency as the primary exciting radiation. This secondary radiation is called dipole radiation because it is coming from two vibrating, oppositely charged particles, which form a dipole.

For a weak light source, like a lamp or sunlight, the oscillation of the created dipoles are harmonic. This means that the response is linear between the vibrational frequency of the light wave and the vibrational frequency of the dipoles [43]. In classical optics the relationship between the induced dielectric polarization of a medium and the applied electric field is linear. This can be described mathematically as

$$\mathbf{P} = \chi^{(1)}\,\mathbf{E} \tag{2.1}$$

where **P** is the induced dielectric polarization, **E** is the electric field. $\chi^{(1)}$ is the linear dielectric susceptibility of the medium. In an isotropic media, such as glass, $\chi^{(1)}$ is a

scalar quantity and its value is the same in all direction of the applied electric field. In a nonisotropic media, like most crystals, the magnitude of polarization varies with the direction of the applied field and χ is expressed as a tensor. The linear susceptibility $\chi^{(1)}$ is related to the index of refraction, n, of the medium by the following equation:

$$\chi^{(1)} = n^2 - 1 \tag{2.2}$$

When a high intensity laser beam passes through a dielectric material such as quartz, the dipoles can no longer respond linearly and they begin to oscillate anharmonically. This is because the driving force (electric field strength) now rivals the electrostatic binding force (Coulomb force) of each atom. The dipoles are not isolated, they are also susceptible to the local fields of their neighbors. The total dipole susceptibility is represented in a tensorial form in order to account for all of the combined local fields. For large values of the electric field $\mathbf{E}$ associated with the laser radiation, the induced polarization can be represented as a series expansion [44].

$$\mathbf{P} = \chi^{(1)} \cdot \mathbf{E} + \chi^{(2)} \cdot \mathbf{E}^2 + \chi^{(3)} \cdot \mathbf{E}^3 + \ldots, \tag{2.3}$$

where $\chi^{(2)}, \chi^{(3)}$, etc. are the second and third order nonlinear optical susceptibilities of the medium.

The expansion can be written as the sum of two terms

$$\mathbf{P} = \mathbf{P}^{L} + \mathbf{P}^{NL} \tag{2.4}$$

where $\mathbf{P}^{L}$ is the linear polarization (equation (2.1)) and the nonlinear polarization, $\mathbf{P}^{NL}$ is given by

$$\mathbf{P}^{NL} = \chi^{(2)} \cdot \mathbf{E}\,\mathbf{E} + \chi^{(3)} \cdot \mathbf{E}\,\mathbf{E}\,\mathbf{E} + \cdots \tag{2.5}$$

The second-order nonlinear effects, the first term in equation (2.5) are not observed in centrosymmetric optical media (media with inversion symmetry) such as glass, liquids, and gases. This is because of the nonlinear response of the dipoles are symmetrical, the effects cancels out. Odd harmonics, like third harmonics of the fundamental wavelength, the second term in equation (2.5) are observed in centrosymmetric crystals. In noncentrosymmetric crystals both even and odd harmonics can be generated [45].

2.2. Second harmonic generation:

In the dipolar approximation the induced second-order polarization **P** depend on the product of the square of the electric field and on the nonlinear third rank susceptibility tensor $\chi^{(2)} = (\chi^{(2)}_{ijk})$. The components of the induced second-order polarization can be written as;

$$P_i(2\omega) = \sum_j \sum_k \chi^{(2)}_{ijk} E_j E_k \qquad (2.6)$$

were i, j, and k corresponds to x, y, and z coordinates.

In the dipolar approximation in order for the $\chi^{(2)}$ bulk tensor not to vanish, the crystal can not have inversion symmetry.The lattice structure of gold is face centered cubic (f.c.c.) and it is centrosymmetric. Therefore, the bulk second order nonlinear susceptibility $\chi^{(2)}$ is zero. However, at the metal-electrolyte interface the symmetry is broken, because there is no center of inversion and second harmonic can be generated.

2.3. Surface nonlinear susceptibility tensor of Au (110)

Surface nonlinear optical susceptibilities are characteristic properties of the material and depend on their electronic structure. In the electric dipole approximation, for visible light, only the valence electrons contributes significantly to the second order nonlinear susceptibilty. Theoretical calculations suggest that the nonlinear polarization occurs in a thin,1-2 Å thick dipole layer [45-47]. Since this dipole layer is very thin, the nonlinear polarizability is sensitive to the changes of the surface charge distribution or to the adsorption of ions or molecules. SHG is therefore sensitive to the symmetry of the surface.

The nonlinear susceptibility depends on the excitation frequency [48]. A more detailed mathematical derivation of nonlinear optical susceptibilities can be found in reference [46,52].

$$\chi^{(2)}_{ijk} = P_i(\omega_1) / E_j(\omega_1) E_k(\omega_1) \qquad (2.7)$$

The nonlinear susceptibility tensor has certain form of symmetry that is related to the surface symmetry. The susceptibility, χ^2 is a third rank tensor with 27 elements. By applying the Neumann principle (the components of a tensor representing a property will remain unchanged under a transformation of the coordinates governed by a symmetry operation for the symmetry group of the material) many of these elements will be reduced to zero and some can be related to each other, this leaves 18 independent, nonvanishing χ_{ijk} elements [53,54]. Equation (2.7) is taken from equation (2.6) where it is evident that interchange of *j* and *k* will not effect this equation and then

$$\chi_{ijk} = \chi_{ikj} \qquad (2.8)$$

i. Surface nonlinear susceptibility tensor elements for an unreconstructed Au (110) with C_{2v} symmetry

The theory used in this work is based on the bulk dielectric continuum developed by Sipe et al. [45] where, in the electric dipole approximation [48-50] the bulk nonlinear susceptibility and second harmonic source disappear. There are other alternative methods developed recently treats SHG [51(a),(b)].

The inversion symmetry is broken at the surface, and therefore a dipolar contribution to SHG exists. Besides, there is a discontinuity in the normal component of the electric field. This gives rise to a big electric field gradient that can generate a large contribution from higher order multipole terms. Both effects are taken into account by an effective surface dipole polarization density given by

$$P_{i,surf}^{(2\omega)} = \sum \Delta_{ijk}^{(2)} E_j E_k \delta(z - z_0^+) \qquad (2.9)$$

where $\Delta_{ijk}^{(2)}$ is the surface susceptibility tensor (in the beam coordinates) and $\delta(z)$ is the Dirac delta function and E is the electric field. For the Au (110)-(1x1) unreconstructed surface with C_{2v} symmetry, equation (2.9) takes the form

$$\begin{pmatrix} P_{x,sur}^{(2\omega)} \\ P_{y,sur}^{(2\omega)} \\ P_{z,sur}^{(2\omega)} \end{pmatrix} = \begin{pmatrix} 0 & 0 & 0 & 0 & \partial_{15} & 0 \\ 0 & 0 & 0 & \partial_{24} & 0 & 0 \\ \partial_{31} & \partial_{32} & \partial_{33} & 0 & 0 & 0 \end{pmatrix} \begin{pmatrix} E_x^2 \\ E_y^2 \\ E_z^2 \\ 2E_yE_z \\ 2E_xE_z \\ 2E_xE_y \end{pmatrix} \tag{2.10}$$

Because of the rotation of the sample it is necessary to transform the surface coordinates (*x,y,z*) to beam coordinates ($\hat{s},\hat{k},\hat{z}$).In Figure 2.1 the unit vectors of the surface coordinates and the beam coordinates are illustrated.

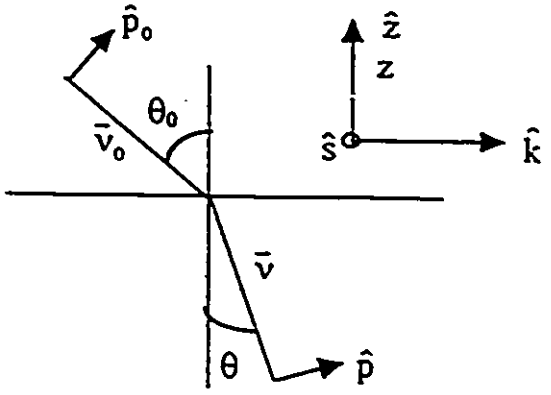

Figyre 2.1. The surface coordinates, *x,y,z* and the beam coordinates $\hat{s}, \hat{k}, \hat{z}$.

Where the $\hat{z}$ direction is taken as the surface normal, and wave vector component perpendicular to $\hat{z}$ is taken as

$$k = \hat{k}|\bar{\nu}_0|sin\theta_0, \tag{2.11}$$

$\bar{\nu}_0$ is the wave vector of the incident field expressed as

$$\bar{v}_0 = k - \omega_0 \hat{z}, \tag{2.12}$$

$\bar{v}$ is the wave vector of the medium, written as

$$\bar{v} = k - \omega \hat{z}, \tag{2.13}$$

$\hat{p}_0$ is the direction of polarization of the incident field given by

$$\hat{p}_0 = \frac{k\hat{z} + \omega_0 \hat{k}}{\omega / c}, \tag{2.14}$$

$\hat{p}$ is the direction of p-polarized light in the medium expressed as

$$\hat{p} = \frac{k\hat{z} + \omega \hat{k}}{n\omega / c} \tag{2.15}$$

where $n = \sqrt{\varepsilon(\omega)}$ the complex refractive index of the medium.

The total SHG intensity including the bulk and surface isotropic and anisotropic contributions for the Au (110) for the unreconstructed surface with a C_{2v} symmetry for the incoming p polarized fundamental and the detected s polarized second harmonic is expressed by equation (2.16) [45]. In the experiment the normalized SHG intensity was measured.

$$I_{ps}^{(2\omega)} = \left| \frac{E_{ps}^{(2\omega)}}{E_p^2} \right|^2 = |A_s|^2 \left(A_{ps} \sin^2 2\phi + B_{ps} \sin 2\phi \sin 4\phi + C_{ps} \sin^2 4\phi \right) \tag{2.16}$$

$$A_{ps} = \left| b_{ps}^{(2)} \right|^2 \tag{2.17}$$

$$B_{ps} = b_{ps}^{(2)} b_{ps}^{*(4)} + b_{ps}^{*(2)} b_{ps}^{(4)} \tag{2.18}$$

$$C_{ps} = \left| b_{ps}^{(4)} \right|^2 \tag{2.19}$$

where A, B and C are the Fresnel factors related to the index of refraction. The b's are the coefficients for bulk anisotropic harmonic field and ϕ is the azimuthal angle between the plane of the incident beam and the <100> axis on the (110) surface.

and A_s is described as $$A_s = \frac{4\pi\tilde{\Omega}}{W_0 + W} \tag{2.20}$$

where $\tilde{\Omega} = \frac{2\omega}{c}$, $W = \left[\tilde{\Omega}^2 \varepsilon(2\omega) - K^2\right]^{1/2}$, $K = 2k$ and $W_0 = \left(\tilde{\Omega}^2 - K^2\right)^{1/2}$

are the equivalent of equations (2.11) to (2.15) for the harmonic field.

By rotating the crystal about its surface normal and relative to the plane of incidence of the exciting beam it is possible to obtain a measure of the rotational anisotropy of $I_{ps}^{(2\omega)}$.

This theory has been applied succesfully to many systems [14,23,24,45]. As an example the SH intensity for Ag (110) in 0.25 M Na_2SO_4 at a potential -0.69 V (vs Ag/AgCl) for s-polarized fundamental and p-polarized second harmonic is shown in Figure 2.2. The Ag (110) surface has a C_{2v} symmetry. The rotational dependence of the SH signal is predicted by Sipes et al. [45] and is given by the following equation.

$$I_{sp} = \frac{E_{sp}^{(2\omega)}}{E_s^2} = A_p (A_{sp} + C_{sp}^{(2)} \cos 2\phi + C_{sp}^{(4)} \cos 4\phi) \tag{2.21}$$

where A_{φ}, $C_{\varphi}^{(2)}$ and $C_{\varphi}^{(4)}$ are the Fresnel factors and ϕ is as defined above. The first term in equation (2.21) describes the isotropic contribution, the second and third terms are the anisotropic surface dipole and bulk quadrupolar contributions. Figure 2.2 shows a good agreement between the theoretical calculation (equation (2.21)) and the measured SH rotational anisotropy. The solid line is the fit of the experimental data using equation (2.21). Notice that the two peaks (from dipolar contribution) are separated by 180^0 which agrees with a cos 2ϕ term in equation 2.21.

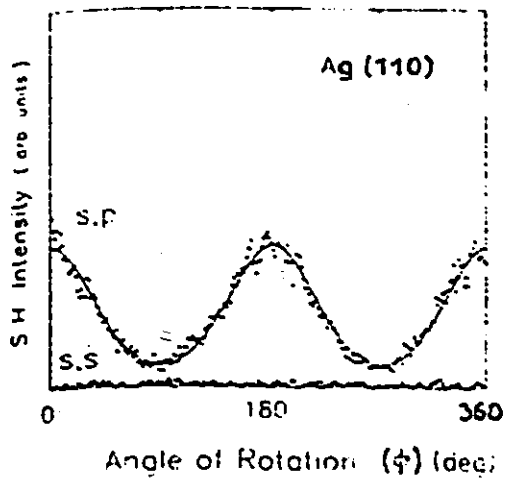

Figure 2.2. An example of a calculated (solid line) and measured (dots) SH intensity for Ag (110) in 0.25 M Na_2SO_4. E=-0.69 V (vs Ag/AgCl). Taken from [24 (b)].

CHAPTER 3: Experimental

3.1.Introduction:

In this chapter the preparation of the Au (110) single crystal electrode and the experimental electrochemical and optical setups are discussed.

For the SHG experiments a Au (110) single crystal was needed which has an ending for an easy attachment of the gold wire and has sufficient mass to resist annealing without melting. The electro-optical cell was designed specifically for the measurement of SHG rotational anisotropy experiments and the optical setup was assembled.

3.2. Preparation of the Au (110) single crystal electrode

The Au (110) electrode was made from pieces of 1mm diameter, 99.9985% Puratronic (Johnson Matthey) gold wire. A gold wire was cleaned in acetone, cut into pieces and about 3.5 g of it was put into a graphite cylinder crucible. The graphite cylinder containing the gold wire pieces was put into a quartz tube that was previously degreased with acetone. The quartz tube was put into a coil of an induction furnace (Elma Engineering, California). The steps in the User's Guide for the induction furnace were followed to melt the gold pieces. According to the instruction the voltage was increased slowly, at a rate of 50 V/minute up to about 700V.

When the top of the quartz tube had a glowing reddish blue flame the voltage was set at 700V for 20 minutes. After that period the voltage was decreased again by 50V/min. to zero volt. The melting process was more difficult when larger pieces of gold were used. The next step was to put the crystal in a solution of aqua regia (approximately 3 volume of HCl to 1 volume of HNO_3) to clean the surface. Aqua regia reacts with the surface gold atoms and forms the $AuCl_4^-$ complex which makes the other single crystal domains edges visible. The shape of the crystal with and without domains is shown in Figure 3.1. In part (A) the sample crystal with the domains are illustrated. This is a polycrystal with many crystallographic domains. In part (B) in Figure 3.1 shows a single crystal with only one domain.

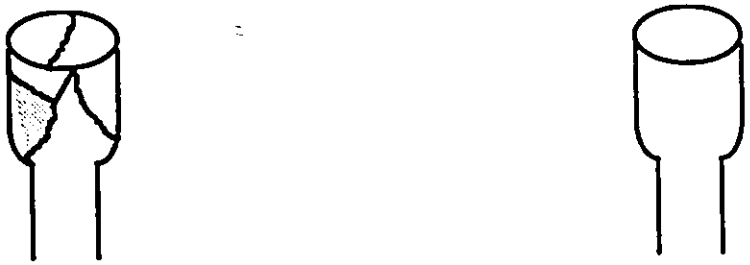

A, Crystal with domains (a polycrystal)

B, Crystal with no domains (a single crystal)

Figure 3.1. The sample crystal with and without domains. The size is expanded for a better illustration.

If domains were observed as shown in Figure 3.1(A), the crystal was remelted again. When only the (110) domain was observed the sample crystal was aligned. The back x-ray scattering Laue technique was used to orient the crystal. The Laue back scattering method uses x-rays which is generated from the continuous spectrum of an x-ray tube operated at about 40 kV. X-rays are electromagnetic waves with wavelength range of 0.1 to 10 nm which are of the order of magnitude of atomic dimensions. X-rays are generated when the electrons from a heated tungsten filament (cathode) of a high vacuum tube are accelerated through the potential difference of several thousand volts and strikes a target (anode). In the target the incident electrons knocks an orbital electron out of an atom. If the ejected electron is from one of the inner shells, then an electron from one of the outer shell will fill the vacancy. The potential energy of the electron decreases as it approaches the nucleus which results in an emission of an x-ray photon having an energy equal to that lost by the electron. The wavelength of the generated x-ray photons are related to ΔE by $\lambda = ch/\Delta E$, where c is the speed of light and h is the Planck's constant. The x-rays are then used to orient the single crystal. The x-rays strike the surface. The parallel layers of atoms in the crystal act as diffraction grating for x-rays in three dimension. For the diffracted waves to be reinforced in certain direction and angle θ, the spacing d between crystal planes must be related to the wavelength λ of the radiation. Bragg's law expresses the relationship between these variables as

$$n\lambda = 2\,d\sin\theta \qquad (3.1)$$

where n is an integer. The angle θ is measured relative to the crystal face [55-57].

X-ray diffraction instrumentation includes a collimated beam of x-rays that is incident on a crystal sample mounted on a goniometer. The interference effect of the back scattered radiation from the different atoms of the gold sample causes the intensity pattern to exhibit minima or maxima in various directions.The diffracted beam is detected with a photographic film. The single crystal structure is deduced by analyzing the positions and intensities of the various spots in the pattern. The experimental setup for X-ray diffraction is described in reference [58]. The distance between the crystal and the film was 6 cm. The photograph was obtained after 20 minutes of irradiation and subsequently developed and analyzed with the aid of a Greninger net. The Greninger net is a projection of a sphere on a flat surface and it is used for reading angular relations on back-reflection x-ray films [59]. The way it is done is the following; the center of the x-ray film is kept on the center of the Greninger net. Then, an intense row of spots are made to coincide with one of the hyperbolas going horizontaly across the chart by turning it through an angle α, which is the angle of the horizontal plane. The angle ϕ can be read off directly from the chart. By adjusting the position of the crystal by the angles α and ϕ the Au (110) plane can be made parallel to the film and perpendicular to the x-ray. The next x-ray film gives the Au (110) pattern at the center; the main zones and the sets of indices assigned to the spots must agree with the stereographic projection having the Au (110) at its center [19]. Afterwards the crystal was cut paralell to the film to have the Au (110) face then it was mechanically polished as described next.

The Au (110) single crystal was held in the goniometer during the polishing process. The mechanical polishing was done first by using different grades of waterproof Si-Carbide polishing papers (Struers).It was frequently rinsed with ultra pure water to get rid of the shed off pieces that could scratch the gold surface. Between each polishing stage the sample was sonicated for about one minute to further clean the surface. A diamond pastes (1μm) and polishing fluid (Metadi) was employed for the next polishing stage. Then the surface was evenly polished and both, the sample and the holder were rinsed well. For the final mechanical polishing stage a finer diamond paste with 0.05 μm was used. Following the mechanical polishing a scratch free, highly reflective, gold surface was obtained.

3.3. Electrochemical Cleaning and Polishing.

Electrochemical cleaning and polishing are the final steps in the preparation of the Au (110) surface. To determine the degree of the electrochemical polishing, and to get a general idea how the cyclic voltammogram (CV) looked like, the Au (110) was put into a 0.01M $HClO_4$ solution. The CV was obtained with the hanging meniscus method [60] in an ordinary electrochemical cell. The hanging meniscus method is used when a CV of a particular crystallographic orientation is required. In this technique only the single crystal face is in contact with the electrolyte solution, otherwise CV would be similar to a polycrystal. The electrode is pulled up above the solution, as illustrated in Figure 3.2.

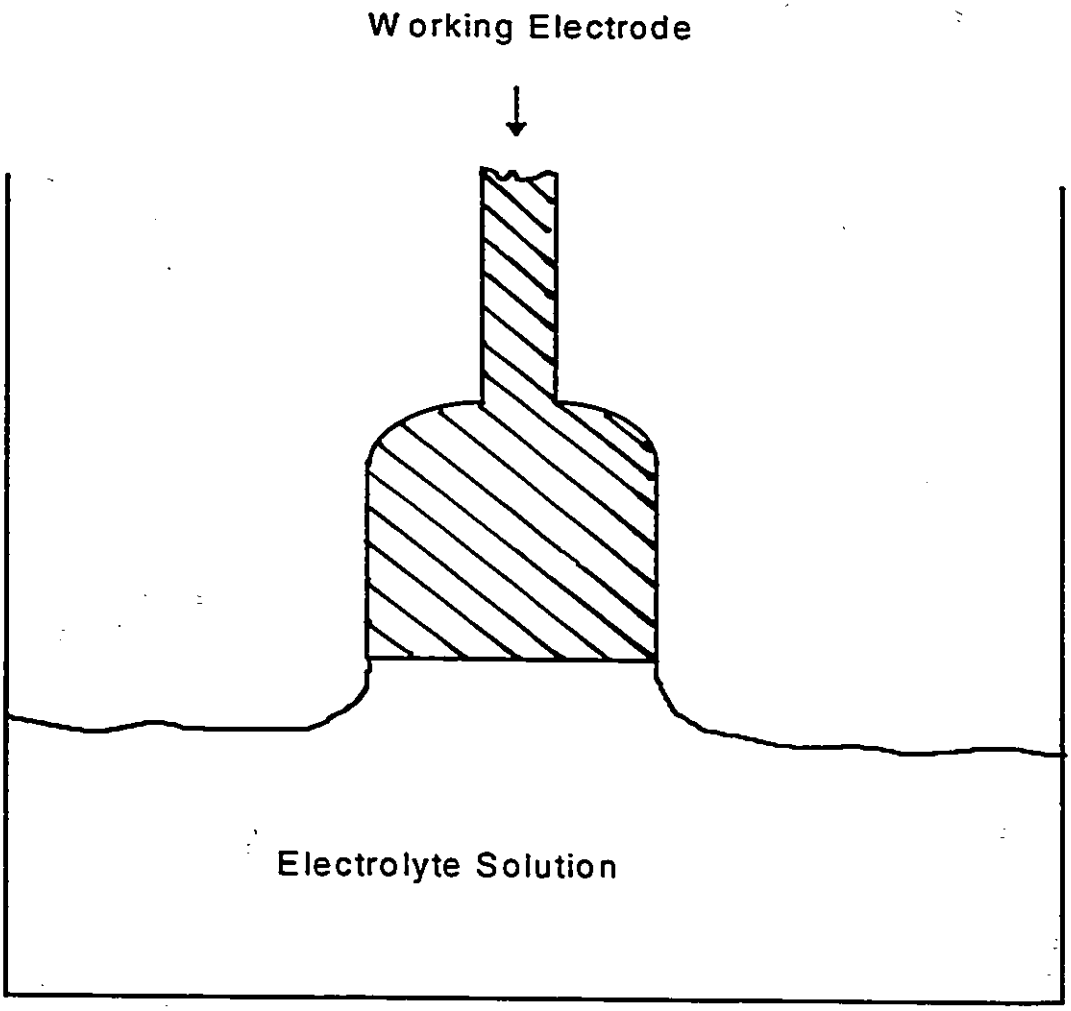

Figure 3.2. The hanging meniscus method. Only the working electrode is shown for clarity.

Annealing is a heat treatment process which has several forms and widely used in industry and research [61]. Annealing relieves stress that may be locked up in the metal. By heating the sample, defects and imperfections can be eliminated and organic contaminations are burned off. In the course of annealing the gold atoms rearranged themselves because of the thermal energy they received from the applied heat. Annealing was specially useful when the CV was close to the literature but some features were not perfect and could not be improved with other methods. Imperfections can be seen in the cyclic voltammograms because CV's are sensitive to the crystallographic orientation and imperfections of the crystal. The gold single crystal was first flame annealed in a natural gas flame for about 45 minutes at a temperature close to the melting point of gold. The temperature was judged from the yellowish red color of the gold. The gold sample was continuously rotated during annealing to avoid melting and insure a homogeneous temperature. The highly reflective surface achieved after mechanical polishing was diminished with annealing. This is because during annealing the defects were collected at the top of the surface that decreased the reflectivity of the gold electrode.

Next, the electrode was polished electrochemically with cyanide. **Extreme** care should be taken when working with cyanide. The Material Safety Data Sheet should be consulted before electropolishing in the cyanide bath. Since the cyanide solution decomposes quickly it should not be kept long and only a small amount should be made. The cyanide solution is prepared in the following way and kept in the fumehood. The composition of the cyanide solution [62]:

6.75g	sodium cyanide
1.5g	potassium sodium tartrate
1.5g	potassium ferricyanide
2.25g	phosphoric acid, concentrated
0.25mL	ammonium hydroxide 15M
100mL	ultrapure water

The solution was continuously stirred with a stirring magnet during the polishing process.

The following polishing procedure was used:

The solution was heated to 60 ^{o}C. The counter and reference electrodes were connected together as described in reference [62]. The potential difference across the two electrodes was set to 6V. The working electrode was the anode. The current converter was set to 20 mA/V.The position of the anode and the cathode were fixed so that the internal resistance in the solution remained constant during the polishing process. The current was switched on and then the Au (110) working electrode to be polished was placed into the cyanide solution. The hanging meniscus method was used to etch only the surface. The cyanide etched a few layers of gold atoms off by forming the dicyanoaurate ion, $[Au(CN)_2]^-$ which is readily formed in the presence of air. Electrochemical polishing must be done carefully because during the polishing process missorientation of the (110) face could increase the number of defects. The time required for electropolishing was determined by the amount of defects on the surface

and the applied current. The duration of electropolishing varied from one to ten minutes. The cyanide treatment gave back a highly reflective surface ready to be put into the electro-optical cell designed for the SHG experiment. The CV obtained in 0.01 M $HClO_4$ with the hanging meniscus (Figure 3.2) at this stage was the same as in the literature [28] (Figure 1.3 and 1.4).

3.4. Description of the electro-optical cell

To perform the SHG experiment with the hanging meniscus method is difficult because it can break during the rotation of the electrode. Rotation of the gold sample was essential because, the SHG intensity was measured as a function of the azimuthal angle. It was therefore necessary to design a cell specially for the SHG experiment.

The electro-optical cell designed has two main parts. A plunger to hold the Au (110) electrode and the cell body with a window (see Fig. 3.3 and 3.4). The plunger could be rotated with a reproducibility of $\pm 3°$ within the cell body and could be moved easily forward and backward. The plunger was made of a glass body with a teflon end attached to it to hold the sample. Figure 3.3 shows the design of the plunger that was to hold the gold single crystal electrode. At the end of the teflon holder a hole was drilled to fit the electrode into it. Inside the plunger from the Au (110) a gold wire made the connection to the potentiostat. The fitting between the glass plunger and the teflon piece was tight in order to prevent the electrolyte from leaking inside the plunger. The fitting of the electrode was done as follows. The Au(110) was annealed again for a few

minutes only to avoid any organic contamination either from air or from handling. Following annealing, for about 45-60 second the sample was cooled then quenched in ultrapure water and a drop was left on the surface in order to protect it. Then the side of the Au (110) crystal was wrapped in a teflon tape and carefully placed into the teflon holder. Great care was taken to make sure the single crystal surface was as parallel as possible to teflon holder. The teflon holder was fitted into the glass plunger and after rinsing with ultrapure water it was placed into the electro-optical cell.

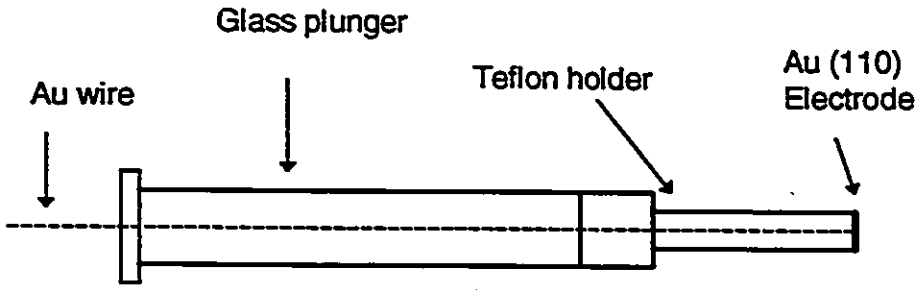

Figure 3.3. The glass plunger and teflon holder for the Au (110) sample which is at the end of the plunger.

The electro-optical cell was made of glass and a teflon part was attached to it to hold a BK7 window (Figure 3.4). The cell was made such a way that a plunger could move in and out and can be rotated as well. On the glass cell body there was pair of inlets for the reference electrode and for the counter electrode. The reference electrode was a saturated calomel electrode (SCE). The counter electrode was a gold foil looped

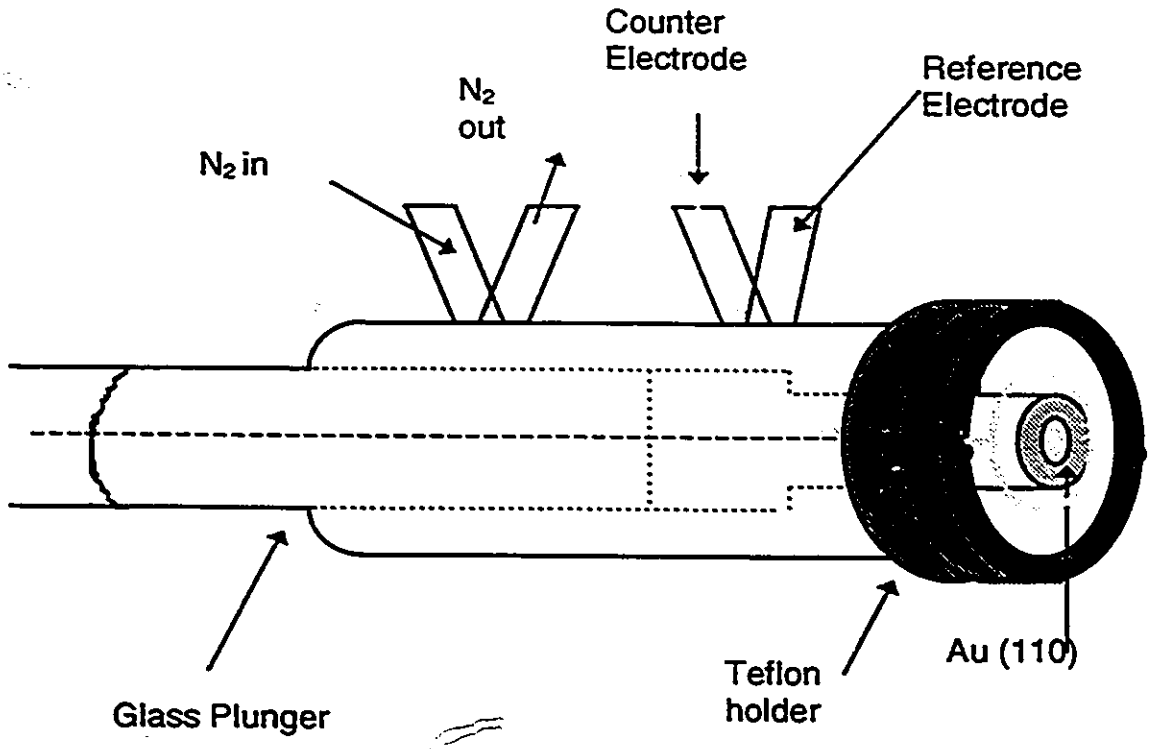

Figure 3.4. The electro-optical cell.

around the working electrode. A gold wire made the connection from the loop to the outside of the cell. The working electrode was the Au (110) single crystal. At the outside end of the plunger a protractor scale was positioned to the aluminium holder to monitor the angle of rotation. The plunger was rotated manually with the aid of a needle to make the angle as precise as possible. To avoid any oxygen interference nitrogen was bubbled through the cell with the aid of another pair of outlets. The cell was mounted to a block of aluminium holder to keep its position fixed during the experiment. First, the cell was rinsed and then filled up with perchloric acid solution. After the potential was cycled at a scan rate of 80 mV/s between -0.3V and 1.4V (SCE) until a clean CV was obtained. During the experiment nitrogen was bubbled through the cell to avoid oxygen interference.

3.5. Cyclic voltammetry

In this section the description of technique of the cyclic voltammetry (CV) is given. Cyclic voltammetry [63-65] is an electrochemical technique used to study electroactive species. In this technique the electrode potential is varied using a linear increase (decrease) of the potential of the electrodes between two previously set values. The CV displays the current on the vertical axis versus the potential on the horizontal axis. Figure 3.5 illustrates the linear variation of potential used as an excitation signal. We used a three-electrode configuration: a working, a counter, and a reference electrode. The working (indicator) electrode is the electrode where the

reaction of interest takes place. The counter (auxiliary) electrode has a larger surface area then the working electrode. Its purpose is to limit the current to the working electrode. The reference electrode was in a separate container and is linked by a Luggin capillary to the cell. This arrangement protects the reference electrode from large current passing through it that could change its potential. It also prevents Cl^- migration which would interfere with our measurement since Cl^- adsorbs on gold.

3.6. Cyclic voltammetry instrumentation

The cyclic voltammetry instrumentation included a waveform generator to produce the triangular excitation signal, a potentiostat to apply the signal to the electrochemical cell, a current-voltage converter to measure the current, and a recording device such as an XY recorder to record the current/potential curve. The potentiostat sets the required potential between the working and the reference electrode and controls the potential applied to the working electrode.

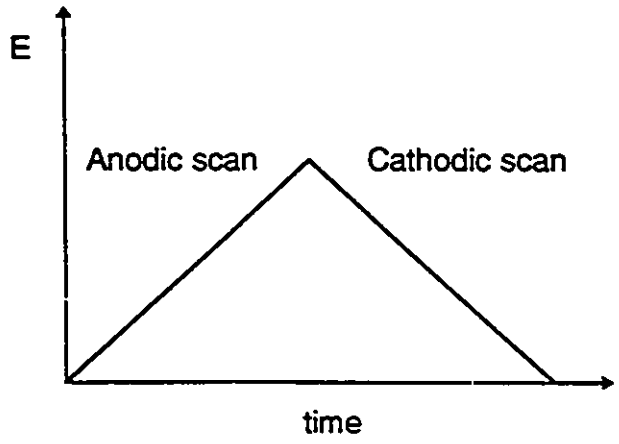

Figure 3.5 Representation of the excitation signal for cyclic voltammetry. One cycle, the forward anodic scan and the reverse cathodic scan is shown.

3.7. Chemicals and solutions

Most of the chemicals used were of the highest purity available to avoid any contamination of the supporting electrolyte since the reconstruction of the surface is very sensitive to contamination. In the majority of the experiments perchloric acid solution was used as supporting electrolyte.

Chemicals used [62]:

$HClO_4$	Made from 70% $HClO_4$. Distilled twice in quartz (Seastar Chemicals)
$KClO_4$	Recrystallized twice (ACS,BDH)
H_2O	Ultrapure (Milli-Q)

KOH to adjust the pH.(Aristar)

All of the solutions were made of Millipore Ultrapure water.

For single crystal electrochemistry not only the solutions have to be extremely pure but also cleaning the glassware is very important. The procedure of cleaning the glassware is outlined below. The glassware was soaked in hot concentrated sulfuric acid and usually left in it overnight to cool. It was then rinsed well in ultrapure water and put into boiling ultrapure water. This step was repeated three times. The glassware was rinsed again and at this stage it was clean enough for the electrolyte solution to be made. Cleaning the glassware this way ensured that impurities from the glass were minimal. The concentration of $HClO_4$ electrolyte used in the experiment was 0.01M. The $KClO_4$ was purchased from BDH (ACS). Since it was not possible to purchase high enough grade it had to be recrystallized twice in water by a general recrystallization procedure. At the end of the recrystallization the solution was cooled slowly to obtain large $KClO_4$ crystals.

3.8. Generation of second harmonic at the interphase.

Since SHG cannot originate from the bulk of centrosymmetric crystals in the dipolar approximation, but at the electrode-electrolyte interface this symmetry is broken and SH can be generated. The metal-electrolyte interface is illustrated in Figure 3.6. In this figure the incoming p polarized fundamental and the detected s polarized second harmonic from the Au (110) surface in the electrolyte solution is illustrated. Gold has a

strong absorption coefficient so its surface reflects most of the incident light both, at 532 nm and 1064 nm.

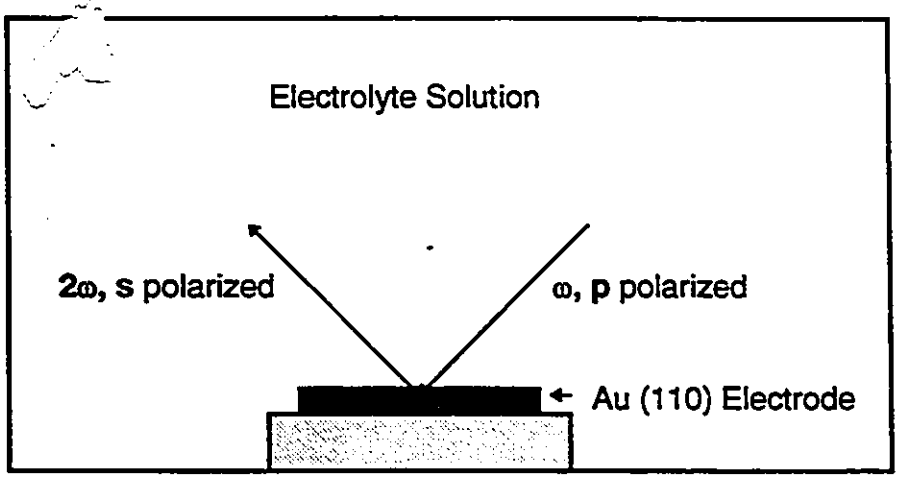

Figure 3.6. Schematic illustration of the incoming p polarized and detected s polarized beams on the Au (110) surface

Only a small portion of the energy of the incident beam is transmitted deeper into the metal surface. The reflection and transmission at the phase boundaries are governed by the Fresnel equations [42].

3.9. Optical Setup:

The assembly and testing of the experimental setup was the most time consuming during this research project. The description of the experimental setup and data acquisition is given in this section. The optical source used for the experiment was an Active Passive, Mode-Locked, Q-switched, pulsed picosecond Nd:YAG laser [66] with a fundamental wavelength of 1064 nm. A picosecond laser was used instead of a nanosecond laser because the peak power and the shorter duration of the pulse gives a more efficient second harmonic optical process. The technique of Q-switching allows the generation of picosecond pulses with more peak power concentrated into a short pulse. Q-switching can be done several ways. In this experiment a saturable absorber, a dye (Exciton, Q-Switch-1 MW 763.33) was used for Q-switching. The way Q-switching works is that, when most of the dye molecules have been excited by intense radiation, the dye loses its ability to absorb more radiation, it becomes saturated. When the dye is saturated it becomes transparent, and the cavity becomes open and lasing occurs. Mode locking is able to produce pulses of picosecond duration. Mode locking allows the random phases in the cavity to be locked together so that they can interfere constructively with each other.The constructive interference occurs as a series of sharp peaks separated by sections of destructive interference. The peak power of the laser is than obtained in a picosecond burst. Active mode locking is achieved using an acousto-optic modulator of the laser cavity. A prism is linked to a transducer (piezoelectric KDP crystal) which is driven by a radiofrequency source at a frequency

c/2L, where c is for the speed of light and L is the cavity length. The transducer sets up standing-wave vibrations in the prism and stabilizes the mode locking process. Mode locking can also be accomplished passively by including a saturable absorber, a dye. When the dye is saturated it becomes transparent and allows a bunch of photons to pass through and travel to the mirror at the other end of the cavity. Immediately the dye shuts down and opens only when the amplified pulse returns from the far end and saturates the dye again. This way the intensity of certain pulses can grow considerably since every time the pulses pass along the cavity they stimulate emission. The active-passive mode locked and Q-switched oscillator pulse train consisted of about 15 individual pulses each separated by the round trip time of about 7ns within the cavity. The duration of each pulse is about 35 ps. The repetition rate was 10 Hz. The 532 nm wavelength generated within the laser is removed with two selective dichroic mirrors before the beam emerged from the laser. A schematic representation of the optical set up is shown in Fig. 3.7. The 1064 nm fundamental beam emerging from the laser is **p** polarized. The **p** polarization is the polarization mode when the electric fields are parallel to the plane of incidence at the surface.Then the beam was passed through a beam splitter where 10% of it was reflected on a pulsed energy meter to monitor the energy and to normalize the SH signal during the experiment. The beam size was reduced by half after it was lead through a reducing telescope. In this experiment only a single pulse was selected from the mode locked pulse train using a single pulse selector (SPS).

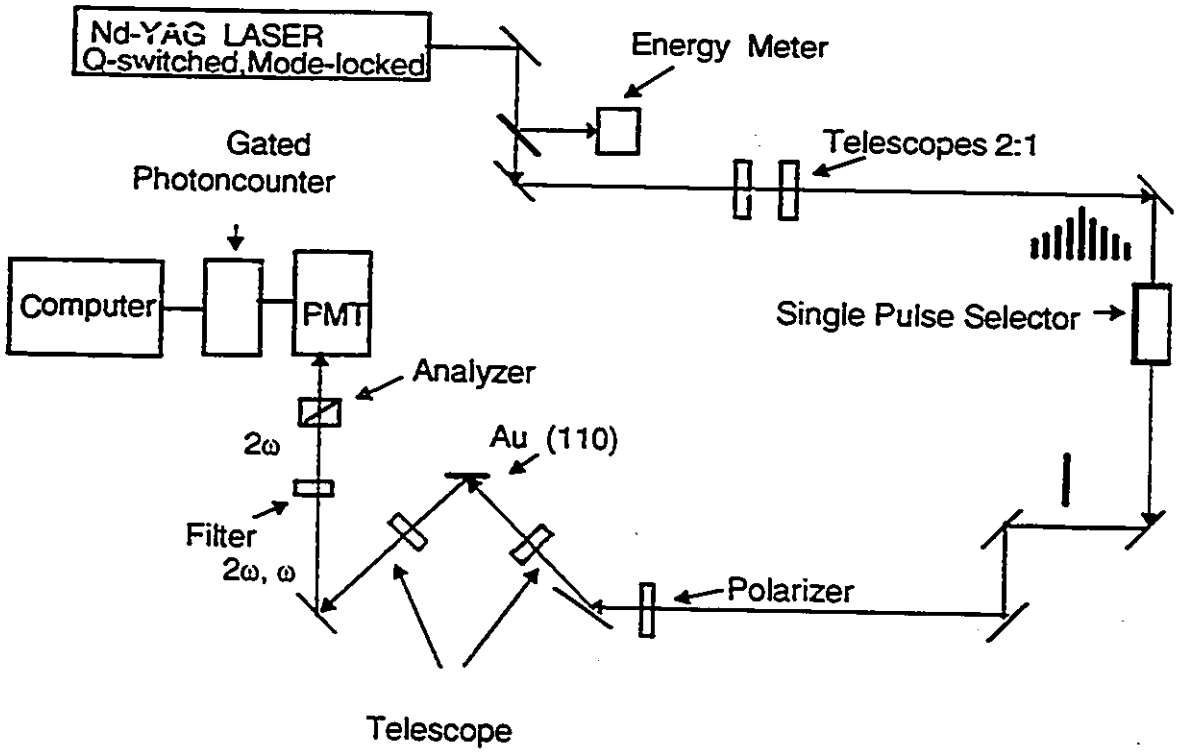

Figure 3.7. Optical setup for SHG spectroscopy.

The reason for using a single pulse is that it cannot heat up the sample as much as the full pulse train would. The SPS unit selects one of the most intense single pulse and rejects the rest of the pulse train. The heart of the SPS unit is the Pockels cell. It is an electro-optical device based on the ability of potassium dihydrogen phosphate (KDP) crystals to rotate the plane of polarization when a high potential difference is applied. The Pockels cell in the SPS unit is triggered by a signal around 6V from the fast photodiode that monitors the output of the laser oscillator. It is best to trigger on the steepest pulse of the pulse train so the neighboring pulses does not cause an early or late triggering of the Pockells cell (KDP crystal). The cable delay of 5 ns/m between the photodiode and the Pockels cell gives an additional delay of the signal so the SPS time window is centered around one of the most intense pulses [67]. The polarizer before the Pockels cell transmits vertically polarized light and the second polarizer, after the Pockells cell transmits horizontally polarized light. When potential is dropped across the Pockels cell the plane of polarization of the laser beam is rotated by 90^0 then the second polarizer can transmit the beam [68]. Therefore, it is possible to switch a single pulse out from the pulse train if the duration of the applied voltage is less than the period between two successive pulses. Because the SPS rotated the beam by 90^0 its polarization changed to **s** (the electric field is perpendicular to the plane of incidence). The energy of the selected single pulse was about 0.35 mJ. The measured energy stability of the selected single pulse was ±10 %. The single pulse was reflected with a set of mirrors and then passed through a polarization rotator. The polarization rotator rotated the plane of polarization by 90^0 back to **p** again (see Figure 3.8). Then the

beam is focused (f=20cm) on the Au (110) sample at an angle of 45^0 from the surface normal. The energy density at the surface was about 3 mJ/cm^2. The SH signal in this configuration is in the same direction as the reflected fundamental beam.The generated second harmonic (532 nm) and the reflected fundamental beams from the Au (110) were collected with a focusing lens (f=15 cm) as illustrated on Figure 3.8. To reject the fundamental the beams were passed through a dichroic mirror and a low pass filter. Then the second harmonic beam was passed through an analyzer. The analyzer blocked the **p** component and transmitted only the **s** component of the generated second harmonic beam. The **s** polarized beam then was focused by a 10 cm focal length lens on the entrance slit of a photomultiplier tube (Hamamatsu R4220P). Photomultiplier tube (PMT) works in such a way when light strikes the photocathode of the PMT, an electron is ejected by the photoelectric effect. The ejected electron is accelerated towards the first dynode. Then secondary electrons are ejected toward the second dynode. This process continues for about 10-14 dynodes where each dynode gains about 4-5 electrons. All together about 10^7 photoelectrons can be collected at the anode by producing a current of 1.6 to 16 mV. The SHG photons were counted with a gated photoncounter (Stanford Sr 400) in a single photon counting mode. The single photon counting mode counts each photon of light individually, and this gives better detectability, higher stability and an improved signal to noise ratio. Photon counting is used at a very low light level. The photon counting system is briefly descibed below.

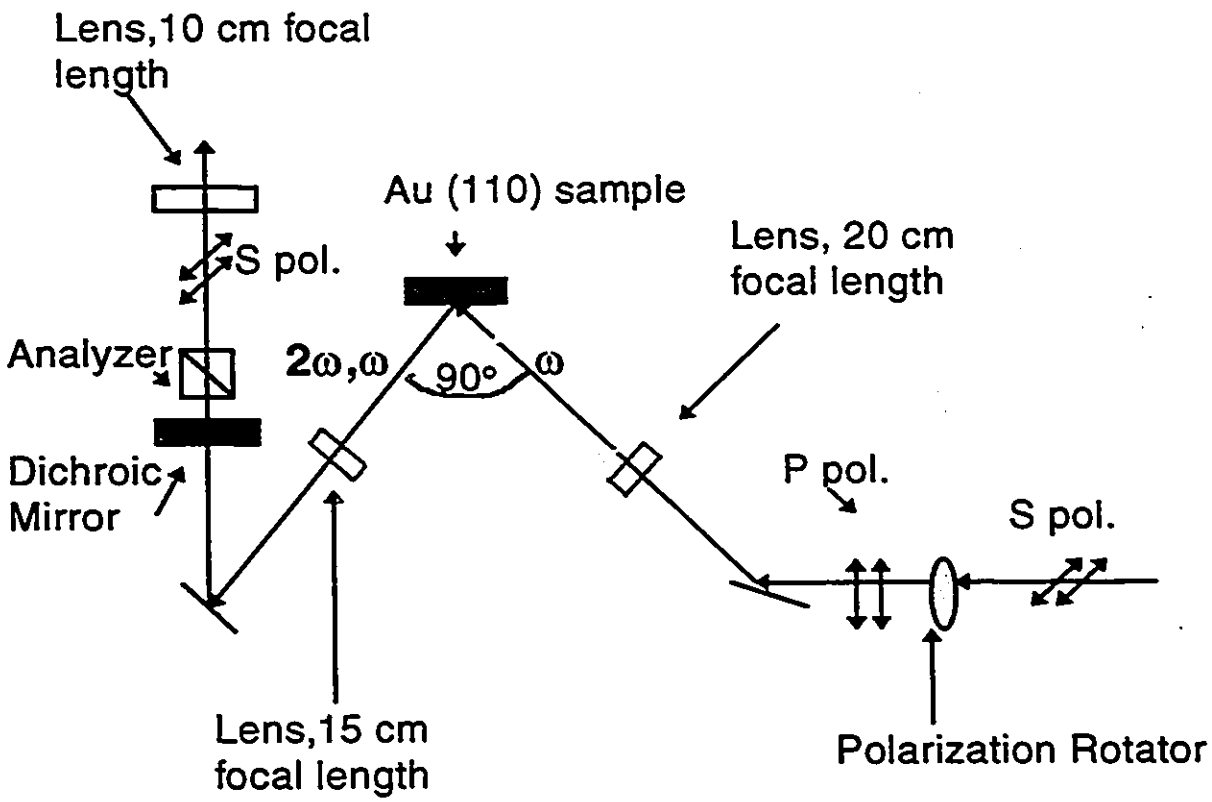

Figure 3.8. The arrangement of the polarizer, analyzer and the lenses at the sample.

The pulses from the PMT are amplified with the main amplifier (A preamplifier can be used before if necessary) and then directed toward the discriminator with a built in IC comparator. In the comparator the pulses are compared with the preset reference voltage and discriminated into two groups. One group of pulses are lower and the other group is higher than the reference voltage. The lower level pulses are eliminated by the

lower level discriminator and the higher level pulses are eliminated by the upper level discriminator. The pulses from the discriminator goes to the pulse shaper and then to the counter. Since lasing occurs 150 ± 10 μs after the flashlamp triggering signal the gate was opened also 140 μs later for 20 μs to count the generated second harmonic photons. The opening of the gates was triggered by the flashlamp trigger input. Gating is used for preventing pulses that occur outside the time interval of interest from being counted and also improves the S/N ratio. The large gate (20 μs) is necessary because the jittering of the dye (the saturable absorber) is about 10 μs, this ensured the detection of all of the SH signals.

Data acquisition for the pulsed energy meter was done with an analog/digital AT-MIO-16 interface board (National Instrument Corporation). The AT-MIO-16 board reads the input signal from the pulse energy meter and translates the analog signal to digital. The data acquisition for the SH intensity from the gated photon counter was performed using a GPIB interface and the Labview software for Windows (National Instrument Corporation). The SH signal was normalized against the energy output of the laser as it is show in equation (3.2).

$$I_{SH_{(2\omega)}}^{Norm} = \frac{I_{SH}^{(2\omega)}}{\left(I_{laser}^{(\omega)}\right)^2} \qquad (3.2)$$

The second harmonic intensity was divided by the square of the laser energy. The way this was done 10% of the incident beam was split to the pulsed energy meter and

read with an A/P card and Labview software program processed the data. The average SH signal level was 20 counts/laser shot. The data collected in this work are an average of 300 laser shots per data point.

Chapter 4: Result and Discussion

4.1. Introduction

In this chapter, the results of the study of the potential induced surface reconstruction of Au (110) electrode in 0.01 M $HClO_4$ by second harmonic generation are presented and analysed.

A summary of previous ex-situ and in-situ studies of the Au (110) surface are discussed below. The ex-situ low energy electron diffraction (LEED) studies in ultrahigh vacuum by Kolb et al. showed that the Au (110) exhibits the (1x2) reconstructed structure at positive charge densities. The reconstructed surface was found to be stable up to +0.9 V (SCE) [37].

The in situ surface X-ray scattering (SXS) study by Ocko et al. [38] did not support the above LEED findings, but confirmed that at negative potential both, the (1x2) and (1x3) reconstruction exists in 0.01 M $HClO_4$. This SXS study reveals an incommensurate first layer relative to the bulk. This occurs because of the mixture of the random distribution of (1x2) and (1x3) reconstructed surface structures. In a salt solution at a negative charge density only the (1x3) reconstruction exists, This observation was also supported by STM measurements which shows that when the potential is more positive than the pzc (-40 mV) in $HClO_4$ the surface reconstruction is lifted. Although, the unreconstructed (1x1) surface contains many islands of adatoms.

Surface reconstruction for Au (110) is also supported by differential capacitance measurements [28,39] which shows a significant hysteresis during the positive and the negative sweep of the potential. This irreversibility in the potential-dependent double-layer capacitance gives another evidence for surface reconstruction (see Fig.1.2).

The in situ scanning tunneling microscopy (STM) study by Weaver et al. [39] confirmed that at above the pzc (-40 mV) the unreconstructed (1x1), while below the pzc mainly the reconstructed (1x2) and (1x3) structures exist in 0.1 M $HClO_4$. The STM result shows dense arrays of parallel strings running in the $<1\bar{1}0>$ direction. The distance between the closest adjacent strings of the (1x2) structure is separated by 8.2 ± 0.3 Å. The string separation for the (1x3) structure is about 16.5 Å. Furthermore, corrugations across the strings are also detected on different STM images. [39]. These images show that the string microstructures are not uniform because they have several short range interruptions. The STM also shows large terraces [69] which contain defects on the Au (110) surface. These are originated from the previous removal and formation of reconstruction. The terraces have well ordered steps that are parallel to the rows and contain the (111) microfacets [39,70,71]. The steps across the rows are highly kinked in the <100> direction.

In this study the SHG rotational anisotropy curves show that the surface symmetry is more complex than the expected. On both surfaces the symmetry elements found are mainly C_s. The data was fitted with three different models which were based on a phenomenological theory [45], and STM [39,70,71] and SXS [38] results.

From the data analysis it was found that there is a significant contribution from the (111) microfacets to the nonlinear susceptibility of the reconstructed and unreconstructed surface.

4.2. Electrochemistry of Au (110) in perchloric acid

A typical cyclic voltammogram obtained before the SHG experiment with the hanging meniscus method in 0.01M $HClO_4$ is shown in Figure 4.1. This voltammogram was obtained at a scan rate of 80 mV/s. The electrochemical processes corresponding to the oxidation and reduction peak potentials were discussed in Chapter 1, where it was also shown that the anodic oxidation and the cathodic reduction peak potentials agree with the literature. The pzc is around -40 mV as expected for the (110) crystallographic orientation for gold where the current is minimum. This means the adsorption-desorption processes are in equilibrium and governed by the Nernst equation. The CV of the double layer on Figure 4.1is symmetric. This means there is no significant contamination neither on the surface nor in the solution close to the electrode. The four main symmetric peaks in the positive potential region, 0.1 V to 0.7 V (SCE) of the double layer corresponds to the adsorption/desorption of ClO_4^- anions in the anodic and cathodic cycle. Since the charge on the electrode is positive it makes sense that the negative ClO_4^- anions are adsorbed on the surface in this potential range. Other voltammetric features include the anodic oxidation peaks between 1.0 and 1.4V (SCE)

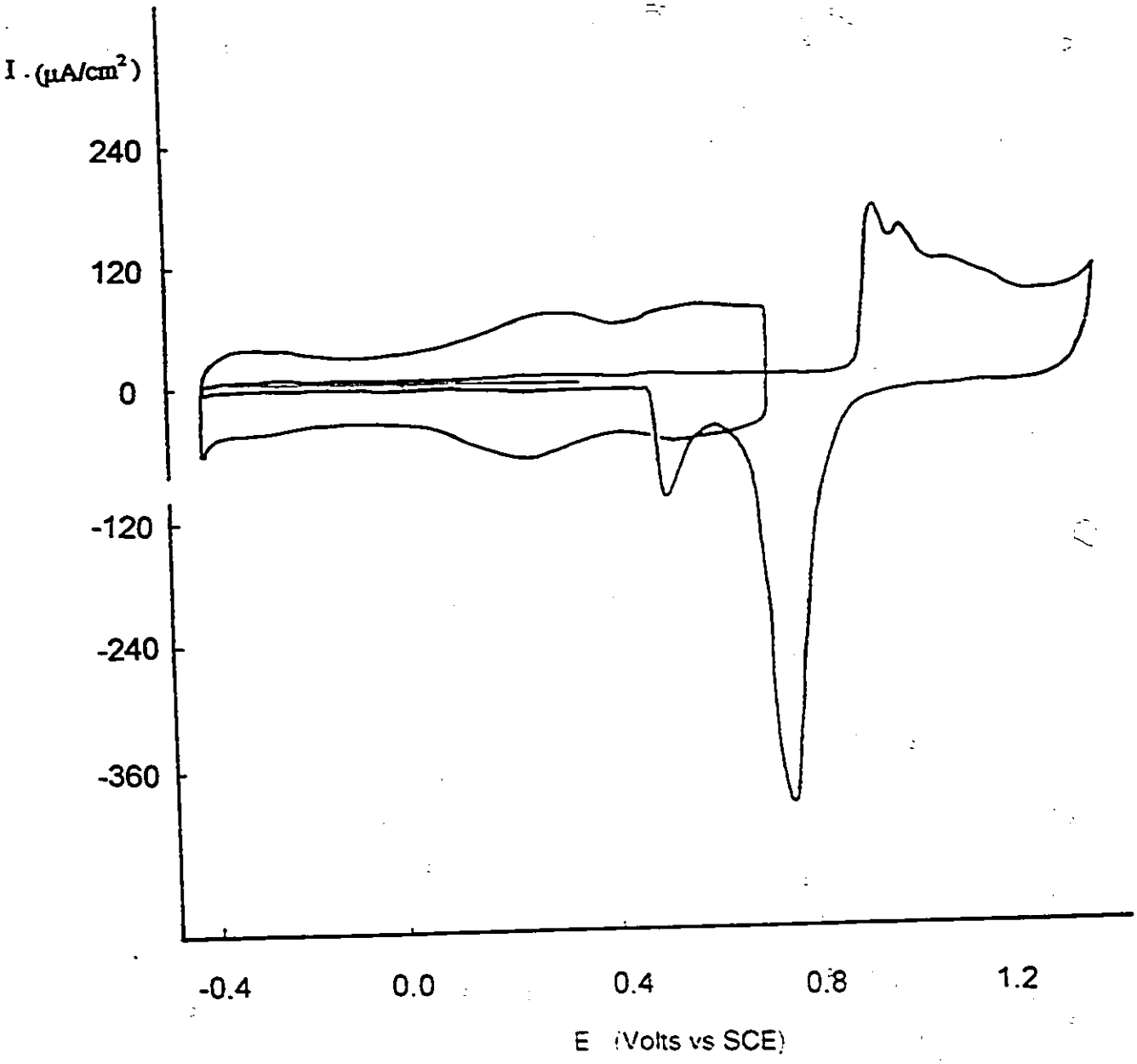

Figure 4.1. Cyclic voltammogram of Au (110) in 0.01 M $HClO_4$ at a scan rate of 80 mV/s. The double layer region is expanded 10 times.

in the upward potential sweep and cathodic reduction peaks around 0.9V (SCE) in the downward potential sweep that were explained in Chapter 1.

4.3. SHG rotational anisotropy of Au (110).

In this section the results of the SHG rotational anisotropy measurement of Au (110) in 0.01 M $HClO_4$ are discussed. The solution was deoxygenated before the experiment for 30 minutes and the CV was recorded. The SH signal was then collected at four potentials; -0.2, +0.4, +0.6 and +0.8V (SCE). The scan rate from one potential to the next was 10 mV/s. The crystal was rotated by 10^0 and the data collection started again at the four potentials described above.

The normalized intensity vs rotational angle and electrode potential was collected with an incoming **p** polarized fundamental and analyzed for **s** polarized second harmonic. The **ps** polarization was used for the SHG measurements because this choice displays a large rotational anisotropy. This data set is the average of four separate runs in four different days. Each of the curves was the average of 300 laser shots. The normalization of the curves were done by dividing the SH intensity with the square of the intensity of the fundamental beam. A linear baseline was chosen close to the lowest count and it was subtracted from the noise before averaging and smoothing the data. The origin of the baseline was from the contribution of optical components.

The reference zero degree was defined as the angle between the plane of incidence of the fundamental light and the <100> direction on the surface (see Figure 4.2).

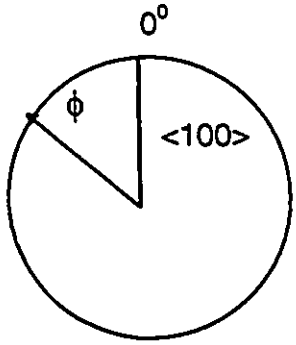

Figure 4.2. The illustration of the zero degree as the <100> plane.
The angle ϕ was rotated by 10^0 increments after each set of potential.

The result of the measured average potential dependence of the SH rotational anisotropy pattern of the Au (110) electrode in 0.01M $HClO_4$ is shown in Figure 4.3. This figure presents the normalized SHG intensity versus the angle of rotation and the applied potential. The applied potentials from the bottom to the top are -0.2, +0.4,+0.6, +0.8 V (SCE). The rotational angle was measured from 0^0 to 360^0 degrees. There are six peaks on these curves with different intensities. There is one intense peak around 30^0, following by two less intense peaks about 80^0 and 120^0. Three smaller peaks at around 220^0, 270^0 and 320^0. Some of the peaks are separated by approximately 60^0 which gives a good indication of the presence of three-fold symmetry elements. The six SH peaks are in agreement with an earlier result obtained by Pettinger et al. in $NaClO_4$ [72].

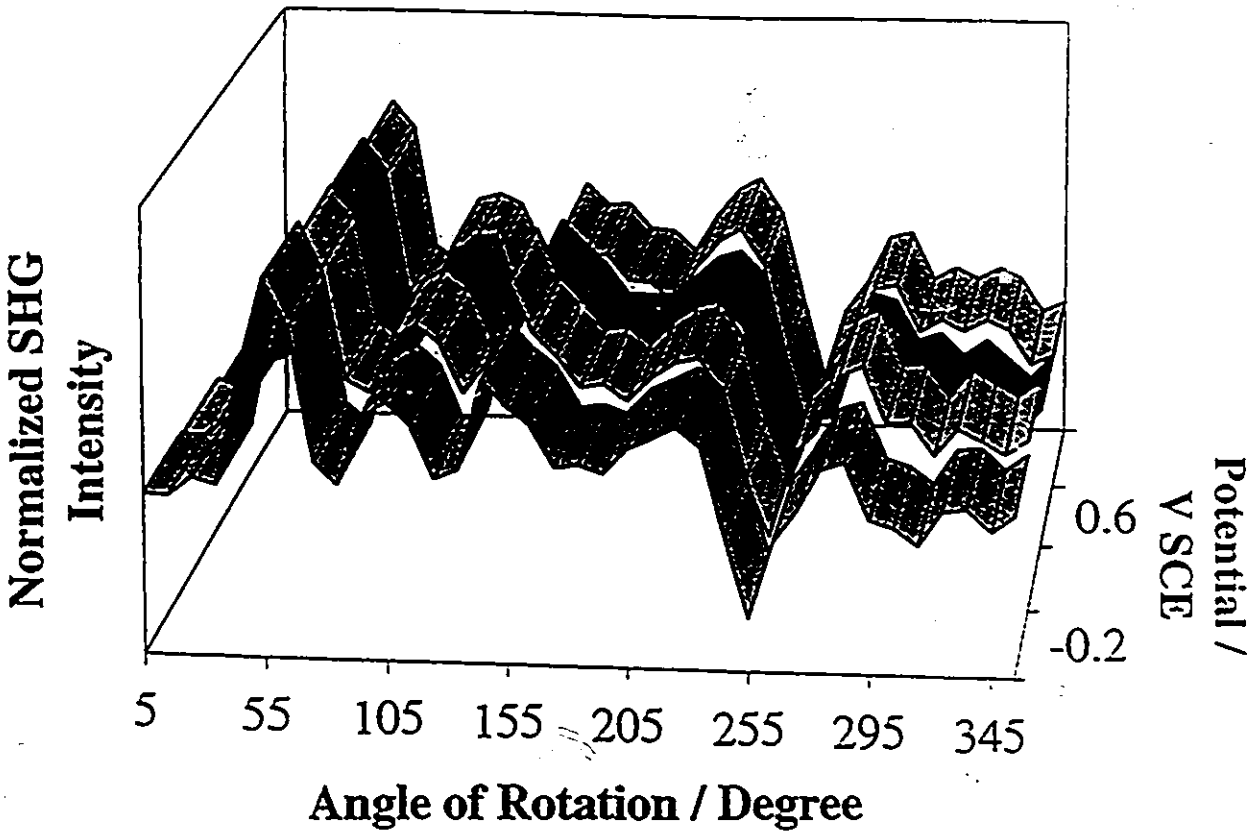

Figure 4.3. The average of the measured rotational anisotropy of Au (110) electrode vs potential for p-polarized fundamental and s-polarized second harmonic in 0.01 M $HClO_4$. The potentials applied were from the bottom to the top of the curve; -0.2 V,+0.4V, +0.6 V, +0.8 V.

An example for a single run of the recorded normalized SH intensity vs rotational angle and electrode potential is shown in Figure 4.4. This is an example of the untreated raw data. For both figures, the estimated number of photons without the baseline was about 5 counts per laser shot. The first SHG data was collected at -0.2V and after about 2 minutes the next reading was taken at +0.4V followed by readings at 0.6V and 0.8V (SCE).

The shape of the average and single SHG rotational anisotropy curves as shown in Figure (4.3) and (4.4) of Au (110) in 0.01 M $HClO_4$ are complex. The curves do not change significantly in the reconstructed (negative potential) region and in the unreconstructed (positive potential) region. This result suggests that, the symmetry of the Au (110) surface is not changing rapidly.

To see a trend relating to the expected surface symmetry the data was fitted by different models. According to the theory developed by Sipe [45] et al. for C_2v symmetry one can expect two or four maxima in the SHG rotational anisotropy curve as was shown in Chapter 2. It was shown that hexagonal (111) microfacets [72] exist along the $<1\ \bar{1}\ 0>$ direction of the reconstructed (1x2) and (1x3) structures. The (111) microfacets can produce threefold symmetry elements i.e. peaks that are separated by 60^0 or 120^0. that are clearly noticable in the SHG rotational anisotropies of the reconstructed Au (110) surface.

Three different models were used to treat the data.

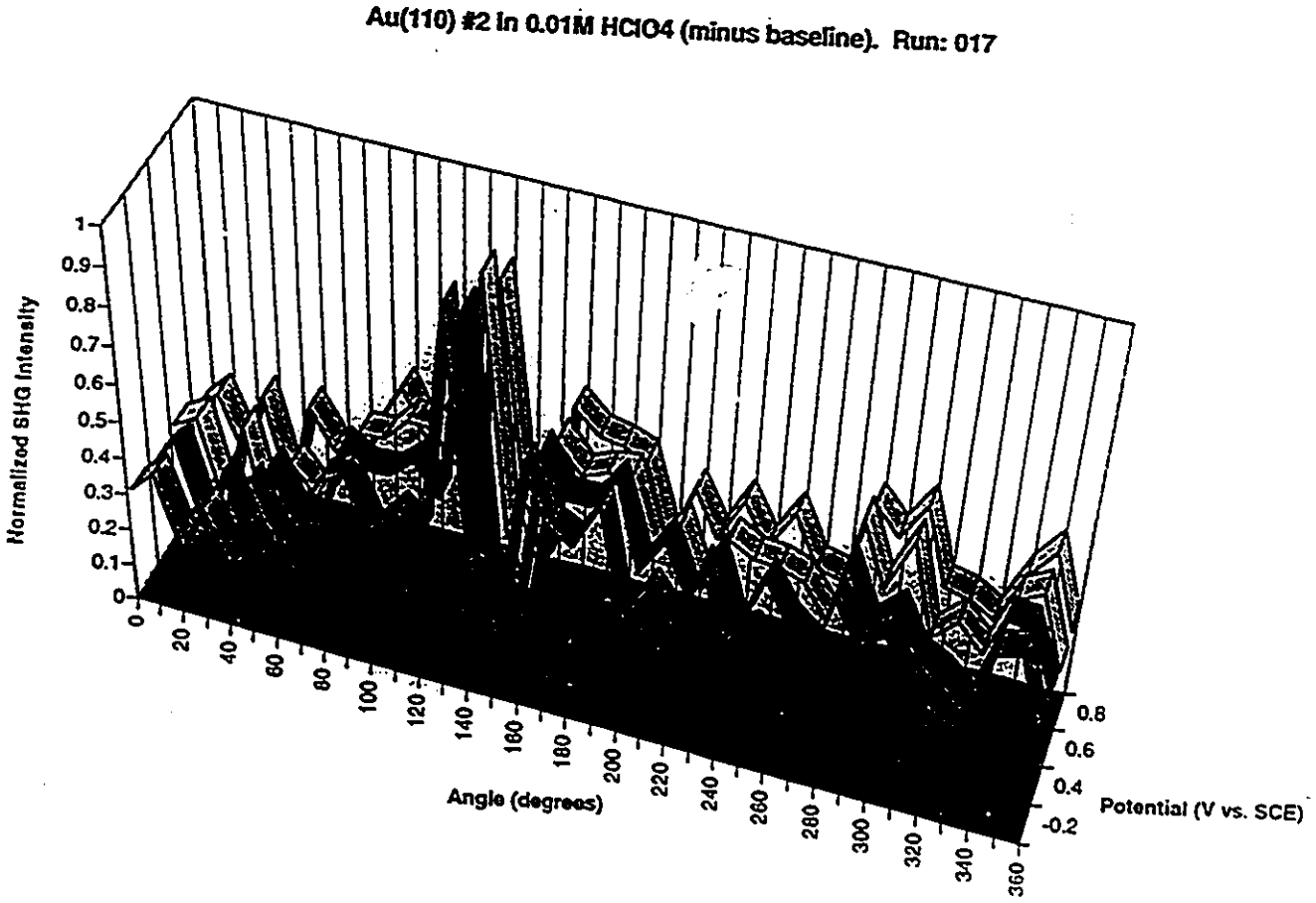

Figure 4.4. A single run for the experimental SHG rotational anisotropy. the condition is same as that for the average runs.

1, The first model was developed by Pettinger et al. [72]. This model takes into account the (111) microfacetting due to the reconstructed (1x2) and (1x3) structures that causes a C_s type SHG anisotropy.

2, The second model was developed in our lab by D.Keefe [75]. It was derived only for C_S symmetry and it did not take into account other symmetry contributions.

3, The third model which is a modification of the second C_S model with an extra threefold component perpendicular to the first one. These models are briefly described below.

4.2. The (111) Microfacetting Model

This model assumes a C_S type symmetry for the reconstructed (1x2) and (1x3) surfaces. The reconstructed surface contains an additional three-fold symmetry element originating from microfacetting. The microfacetting model for SHG intensity for **p** polarized fundamental and **s** polarized second harmonic is given below in equation (4.1).

$$I_{ps} \propto | a' \sin\phi + b' \cos\phi + c \sin 2\phi + d' \sin 3\phi + e' \cos 3\phi |^2 \qquad (4.1)$$

where ϕ is the angle between the plane of the incident beam and the <100> axis on the (110) surface.

$a' = a \cos \alpha_1$

$b' = b \sin \alpha_1$

$d' = d \cos \alpha_3$

$e' = e \sin \alpha_3$

where α_1 and α_3 are the angles of the direction of the (111) microfacets whose orientation is different from the $<1\bar{1}0>$ axis. The angles α_1 and α_3 are adjustable parameters and they also introduce the cos ϕ and cos 3ϕ terms. The sin ϕ and the sin 3ϕ terms are associated with the pseudo-C_{3v} symmetry of the (111) microfacets.

4.3. The C_S model

This model corresponds to a (110) surface which had a C_{2v} symmetry initially but because of the random distribution of the (1x2) and (1x3) reconstruction, the symmetry changes to a C_S symmetry.The mirror plane of the C_S symmetry is along the <100> direction. The susceptibility tensor in a tensor notation for the C_S symmetry is shown in equation (4.2)

$$\chi^{(2)} = \begin{pmatrix} 0 & 0 & 0 & 0 & \chi_{xxz} & \chi_{xxy} \\ \chi_{yxx} & \chi_{yyy} & \chi_{yzz} & \chi_{yyz} & 0 & 0 \\ \chi_{zxx} & \chi_{zyy} & \chi_{zzz} & \chi_{zyz} & 0 & 0 \end{pmatrix} \qquad (4.2)$$

Equation (4.2) is written in terms of the surface coordinates (*x,y,z*), these are transformed to the beam coordinates ($\hat{s}.\hat{k}.\hat{z}$) [45] (see Figure 2.1). The *x* direction is the $<1\bar{1}0>$ axis, the *y* direction is the <100> direction and the *z* direction is perpendicular to the surface.

This transformation from surface coordinates to the beam coordinates means a change from one set of mutually perpendicular axes to another set with the same origin.

After transformation the susceptibility tensor in the beam coordinates is expressed as Δ'. The elements of Δ' for the C_S model is listed in Table 4.1. All other elements not shown are zero. By knowing the elements of the second order susceptibility tensor the SHG intensity for the C_S symmetry can be obtained.

Table 4.1

Second order surface tensor elements of the susceptibility tensor in terms of beam coordinates for a C_s surface.

$$\Delta'^{(2)}_{xxx} = -\tfrac{1}{2}\left(\chi_{xxy} + \frac{\chi_{yxx} + 3\chi_{yyy}}{2}\right)\cos\phi + \tfrac{1}{2}\left(\chi_{xxy} + \frac{\chi_{yxx} - \chi_{yyy}}{2}\right)\cos 3\phi$$

$$\Delta'^{(2)}_{xxy} = \Delta'^{(2)}_{xyx} = \tfrac{1}{2}\left(\chi_{xxy} - \frac{\chi_{yxx} - \chi_{yyy}}{2}\right)\sin\phi - \tfrac{1}{2}\left(\chi_{xxy} + \frac{\chi_{yxx} - \chi_{yyy}}{2}\right)\sin 3\phi$$

$$\Delta'^{(2)}_{xxz} = \Delta'^{(2)}_{xzx} = \left(\frac{\chi_{xxz} + \chi_{yyz}}{2}\right) - \left(\frac{\chi_{xxz} - \chi_{yyz}}{2}\right)\cos 2\phi$$

$$\Delta^{(2)}_{xxy} = \tfrac{1}{2}\left(\chi_{xxy} - \frac{3\chi_{yxx} + \chi_{yyy}}{2}\right)\cos\phi - \tfrac{1}{2}\left(\chi_{xxy} - \frac{\chi_{yxx} - \chi_{yyy}}{2}\right)\cos 3\phi$$

$$\Delta^{(2)}_{xyz} = \Delta^{(2)}_{xzy} = \left(\frac{\chi_{xxz} - \chi_{yyz}}{2}\right)\sin 2\phi$$

$$\Delta^{(2)}_{xzz} = -\cos\phi\chi_{yzz}$$

$$\Delta^{(2)}_{yxx} = -\tfrac{1}{2}\left(\chi_{yxy} - \frac{3\chi_{yxx} + \chi_{yyy}}{2}\right)\sin\phi - \tfrac{1}{2}\left(\chi_{yxy} + \frac{\chi_{yxx} - \chi_{yyy}}{2}\right)\sin 3\phi$$

$$\Delta^{(2)}_{yxy} = \Delta^{(2)}_{yyx} = -\tfrac{1}{2}\left(\chi_{xxy} - \frac{\chi_{yxx} - \chi_{yyy}}{2}\right)\cos\phi + \tfrac{1}{2}\left(\chi_{xxy} + \frac{\chi_{yxx} - \chi_{yyy}}{2}\right)\cos 3\phi$$

$$\Delta^{(2)}_{yxz} = \Delta^{(2)}_{yzx} = \left(\frac{\chi_{xxz} - \chi_{yyz}}{2}\right)\sin 2\phi$$

$$\Delta^{(2)}_{yyy} = \tfrac{1}{2}\left(\chi_{xxy} + \frac{\chi_{yxx} + 3\chi_{yyy}}{2}\right)\sin\phi + \tfrac{1}{2}\left(\chi_{xxy} + \frac{\chi_{yxx} - \chi_{yyy}}{2}\right)\sin 3\phi$$

$$\Delta^{(2)}_{yyz} = \Delta^{(2)}_{yzy} = \left(\frac{\chi_{xxz} + \chi_{yyz}}{2}\right) + \left(\frac{\chi_{xxz} - \chi_{yyz}}{2}\right)\cos 2\phi$$

$$\Delta^{(2)}_{yzz} = \sin\phi\chi_{yzz}$$

$$\Delta^{(2)}_{zxx} = \left(\frac{\chi_{zxx} + \chi_{zyy}}{2}\right) - \left(\frac{\chi_{zxx} - \chi_{zyy}}{2}\right)\cos 2\phi$$

$$\Delta_{xy}^{(2)} = \Delta_{yx}^{(2)} = \left(\frac{\chi_{xx} - \chi_{yy}}{2}\right)\sin 2\phi$$

$$\Delta_{xx}^{(2)} = \Delta_{zx}^{(2)} = -\cos\phi\chi_{yx}$$

$$\Delta_{yy}^{(2)} = \left(\frac{\chi_{xx} + \chi_{yy}}{2}\right) + \left(\frac{\chi_{xx} - \chi_{yy}}{2}\right)\cos 2\phi$$

$$\Delta_{yx}^{(2)} = \Delta_{zy}^{(2)} = \sin\phi\chi_{yx}$$

$$\Delta_{zz}^{(2)} = \chi_{zz}$$

The SHG intensity for p polarized fundamental and s polarized second harmonic is shown in eqn. (4.3).

$$I_{ps} \propto \left|e\sin 2\phi + f\cos\phi + g\cos 3\phi\right|^2, \tag{4.3}$$

$$e = f_c f_s(\chi_{xxz} - \chi_{yyz}), \tag{4.4}$$

$$f = \tfrac{1}{2} f_c^2(\chi_{xxy} - \frac{3\chi_{yxx} + \chi_{yyy}}{2}) - f_s^2\chi_{yzz}, \tag{4.5}$$

$$g = -\tfrac{1}{2} f_c^2(\chi_{xxy} - \frac{\chi_{yxx} - \chi_{yyy}}{2}). \tag{4.6}$$

where ϕ is the angle between the plane of the incident beam and the <100> axis on the Au (110) surface. f_c and f_s are the Fresnel factors, *e*, *f* and *g* are complex quantities and *g* was taken as a real quantity to treat the data.

4.4. Modified C_S model

The SHG intensity for the modified C_S model is given by the following equation to which an extra 3-fold *sin* component was added because of the microfacetting of the Au (110) reconstructed surface.

$$I_{ps} \propto | h \sin 2\phi + i \cos \phi + j \sin 3\phi + k \cos 3\phi |^2 \qquad (4.7)$$

where *h, i, j* are complex quantities and *k* is taken as a real quantity for fitting purposes. The definition of ϕ is as before. The modified C_S model includes the extra three-fold component, where this second source of three-fold symmetry is perpendicular to the other C_S three-fold symmetry source. This assumption is based on the fact that the Au (110) reconstructs along the <100> direction and the long chains of atoms are built in the $<1\,\bar{1}\,0>$ direction. Consequently it is possible to have two sources of nonlinear susceptibilities along these directions.

4.5 Fitting of the experimental data

The method of nonlinear least squares was used to fit the data. The data was fitted using the C_S model equation (4.3), the microfacetting model equation (4.1) and the modified C_S model equation (4.7). The fitting parameters of these equations and the standard deviation are shown in Table 4.2. The result of the fitting is shown in Figure 4.5. As can be seen in Figure 4.5 (b), the trend revealed in the experimental SHG data at -0.2 V in Figure 4.5 (a) cannot be reproduced with the C_S model. The position and the number of peaks obtained for the rotational anisotropy curves are different.

The fitting obtained with the microfacetting model is shown in Figure 4.5 (c). This fit is closer to the experimental rotational anisotropy data. The number and the positions of the peaks resemble more the actual data. The extra one and three-fold anisotropy source gives sufficient flexibility to the fitting functions to provide peaks with different intensities. However, in this model the meaning of the adjustable parameters, α_1 and α_3, is not exactly known. The data was well fitted with the modified C_S model (Figure 4.5 (d)). which also gives support to that the threefold anisotropy is originating from the C_S symmetry of the surface and also from the (111) microfacets.

The magnitude of parameters versus the applied potentials for equation (4.7) are plotted for the modified C_S model (Figure 4.6). This graph shows that the symmetry of the SHG rotational anisotropy at -0.2 V (SCE) is mainly three-fold because the magnitude of the three-fold components are the largest.

Table 4.2

Parameters of least squares fit of experimental data at -0.2V.

Parameter	Value
Microfacetting Model	
a'	-0.1017 + i0.1718
b'[a]	-0.1248 + i0.2108
c	-0.3210 - i0.0635
d'	0.1147
e'	0.0517
Standard deviation	0.073
C_s model	
e	-0.1266 + i0.3473
f	0.0338 + i0.0667
g	0.2558
Standard deviation	0.083
Modified C_s model	
h	-0.1257 + i0.1839
i	-0.0515 + i0.0202
j	-0.1470 - i0.2414
k	0.3080
Standard deviation	0.065

[a] Note that from eqns. (4.1), b_i' was held fixed to $b_i' = \frac{a_i b_r'}{a_r'}$.

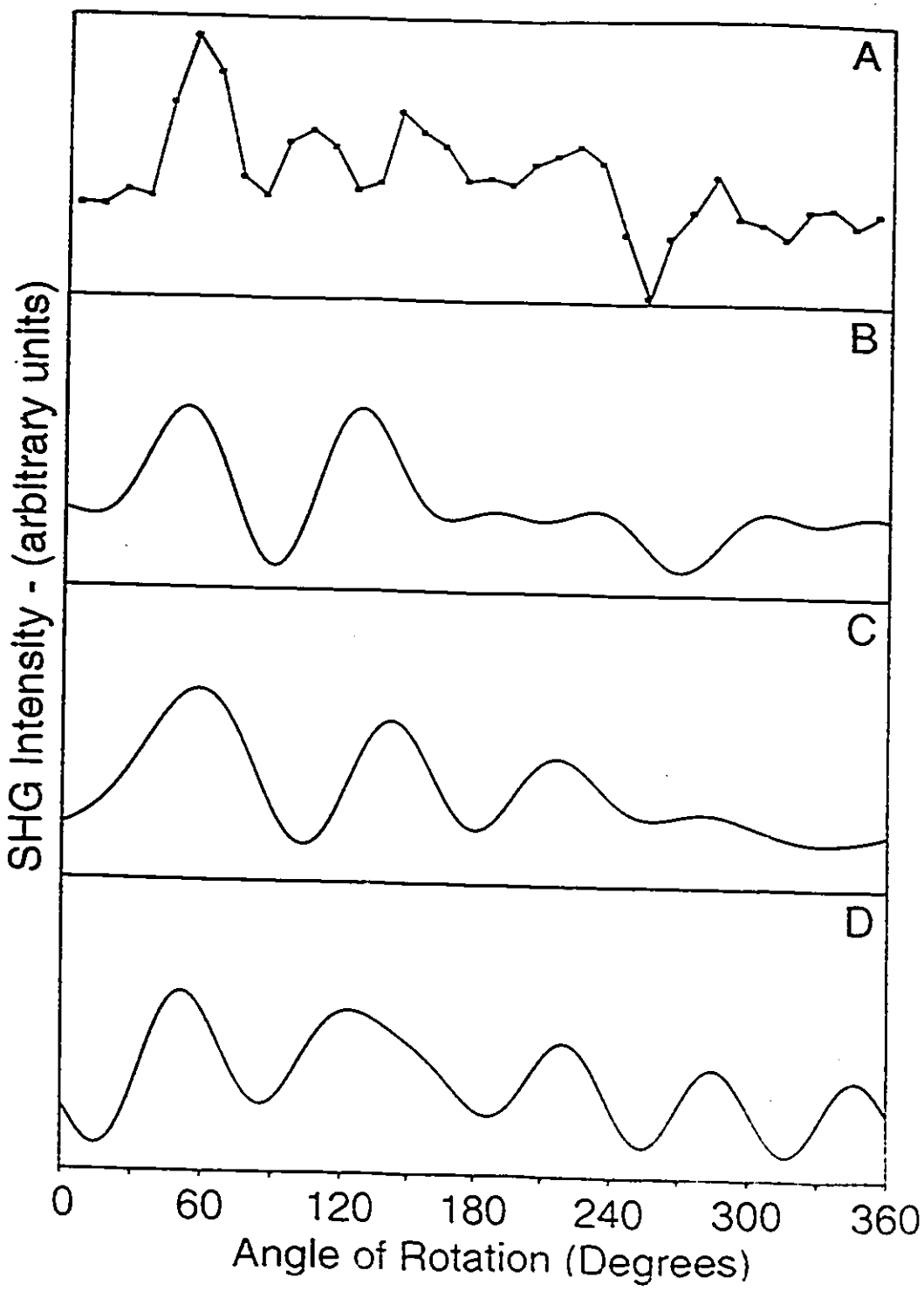

Figure 4.5. Rotational anisotropy of Au (110) electrode in 0.01 M $HClO_4$ at -0.2 V (SCE). (A) Experimental data. (B) Least square fit of C_S model (eqn. 4.3). (C) Least square fit of the microfacetting model (eqn. (4.1)). (D) Least square fit of the modified C_S model (eqn. (4.7)).

The top two curves in Figure 4.6, where (°) represents the sin 3ϕ term and ($^{\Delta}$) represents the cos 3ϕ term, are similar in magnitudes and they correspond to the two perpendicular sources of the three-fold symmetry. The third point from the top ($^{\square}$), represents the magnitude of the sin 2ϕ term. In the modified C_S model the two-fold component relates to the domains of pseudo-C_{2v} symmetry. In the bottom curve ($^{\blacksquare}$) represents the magnitude of the cos ϕ term that is the one-fold symmetry component of the rotational anisotropy. The one-fold contribution is significantly smaller than the two and three-fold components. In the modified C_S model the magnitude of the parameters suggests that the surface nonlinear response of the reconstructed surface is coming from the structures having a pseudo-C_{2v} and a pseudo-C_{3v} symmetry.

The modified C_S model shows that the appearance of the three-fold symmetry to some extent can originate from a surface which has a C_S symmetry. Consequently, the magnitude of the three-fold component might not originate only from the (111) microfacets of the reconstructed surface, but some other symmetry sources related to the C_S symmetry. Pettinger et al. [72] suggested that the main source of the three-fold rotational anisotropy is from the (111) microfacets. In the modified C_S model developed in our lab the directions of the two three-fold sources have definite directions; the second three-fold source is perpendicular to the other three-fold symmetry source. While in the microfacetting model the angle was used as a fitting parameter. STM results [39,70,71] show two main axes of symmetries in the $<1\bar{1}0>$ and <100> directions which are perpendicular to each other. Also, surface relaxation [39,73] which occur with surface reconstruction can modify the (111) microfacets.

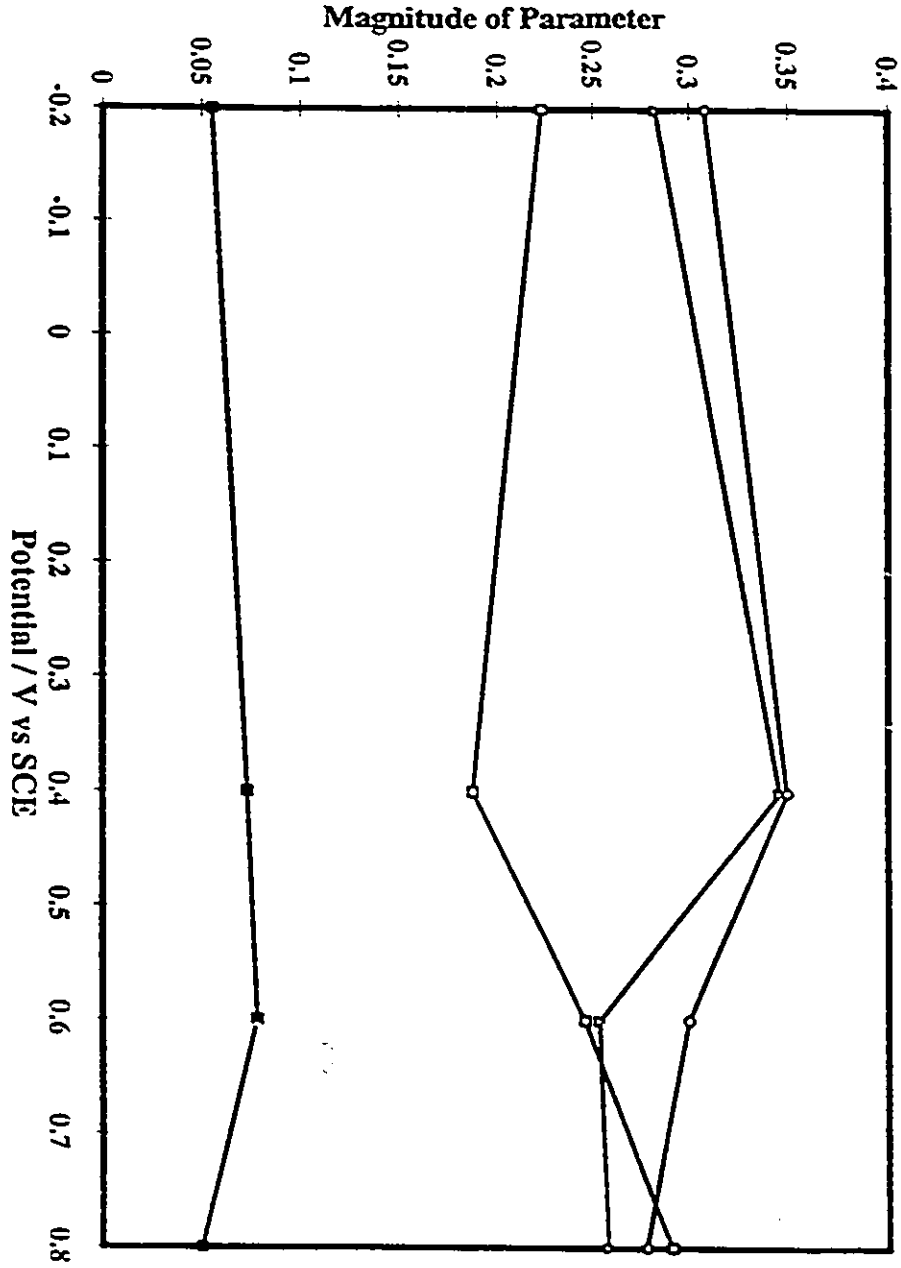

Figure 4.6. The magnitude of the fitting parameters for the modified C_S model vs applied potential. (°) sin 3ϕ, (Δ) cos 3ϕ, (□) sin 2ϕ, (■) cos ϕ

In this case the local structure of the (111) microfacets would have two mirror planes where one of the planes is coincident with the mirror plane of the C_s model and the other is perpendicular to it.

As shown in Figure 4.3 and 4.4 there is little change in the second harmonic rotational anisotropy curves in the potential range studied. Furthermore, the magnitudes of the fitted parameters do not change significantly in this potential range (Figure 4.6). Pettinger et al. observed similar result in $NaClO_4$ [72] where the rotational anisotropy was relatively invariant from -0.2 V (SCE) to the onset of oxide formation. These results suggests that the nature of the cation does not modify the SHG rotational anisotropy. According to these SHG studies in perchlorate electrolytes, the nonlinear susceptibility response of the Au (110) surface does not change significantly from the reconstructed to the unreconstructed surface. The magnitude of both three-fold components (the two top curves (°) in Figure 4.6) are similar and hardly change between -0.2 and +0.4 V. In this potential range where reconstruction should be lifted according to STM. The magnitude of these two three-fold symmetry components decrease between +0.4 and +0.8 V where the surface is unreconstructed [39,70,71]. This suggests that if the three-fold symmetry component originates primarily from the (111) microfacets the number of atoms in the (111) microfacets would not change to a large extent in this potential range. However, the magnitude of the two-fold component which is related to the pseudo-C_{2v} symmetry varies differently. It decreases between -0.2 and +0.4 V and increases between +0.4 and +0.8 V (SCE). The small increase of the two-fold component and decrease of the three-fold component can be explained

with the increase of the well ordered unreconstructed regions on the Au (110) electrode surface.

Since the variations of the magnitudes of the components in perchlorate solutions are small, the lifting of the reconstruction should be a gradual process. A gradual phase transition is also suggested by differential capacitance measurement [39] where in the double layer region there is a large hysteresis in the capacitance curves between positive and negative going potential sweep within -0.3 V and +0.7 V (SCE). If the hysteresis is related to the reconstruction process then the reconstruction would occur over a wide potential range. Based on the STM results [39] the hysteresis could be explained with surface disorders, such as steps, defects, islands and microfacets. An STM study [71] reveals that in 0.1 M $HClO_4$ the Au (110) surface reconstruction exits only at potentials more negative than +0.05 V (SCE). The unreconstructed electrode surface contains a large number of structural defects, like islands on larger terraces and (1x3) elements. The defects are related to the preceding removal and formation of the reconstructed surface. The STM study [71] also says that the reconstruction occurs via local nucleation and does not support the gradual phase transition, but agrees with that at positive charge densities e.g; above +0.1 V (SCE) the surface is largely unreconstructed.

To compare the present and previous SHG and STM informations at a potential of +0.1 V (SCE) the conclusion is that SHG must be more sensitive than STM to the presence of defects, steps, islands and (111) microfacets. However, the STM study [71] shows that the amount of defects are only a few percent and accordingly this cannot be

the main source of the SHG rotational anisotropy. Other factors, such as the quality of pretreatment of the electrode surface especially the flame annealing process along with the purity of the electrolyte solution can have a significant effect on the Au (110) surface reconstruction. This could include the formation of larger (111) microfacets which depends on flame annealing. It is also possible that the removal of defects on the not well ordered unreconstructed surface could have contributed to the measured SHG rotational anisotropy on the electrode surface. According to STM measurement these surface imperfections are removed slowly [71] or not at all at more positive potentials. This agrees with the gradual change from the reconstructed to the unreconstructed surface that was observed in this experiment.

It should be noted that when more strongly adsorbing electrolytes, such as halides are used, the SHG and STM observations are in close agreement. For instance, the adsorption of bromide ions in $NaClO_4$ supporting electrolyte results in a lifting of the (111) microfacetting. This is suggested by the relatively sharp disapperance of the three-fold symmetry component (see Figure 3b of Ref. [72]). The transition with the Br^- adsorption is more obvious then the results of this experiment with the weakly adsorbing perchlorate anion. Therefore we believe that SHG is following the surface reconstruction and not the amount of defects. The results suggest that the SHG is detecting the slow transition from a reconstructed to an unreconstructed Au (110) surface which causes significant change between 0.4 and 0.8 V (SCE) in 0.01 M $HClO_4$ electrolyte. The slow transition from a reconstructed (1x2)/(1x3) to the unreconstructed (1x1) surface can be due to the low mobility of the

top layers of atoms in a weakly adsorbing electrolyte. The formation and lifting of reconstruction is not as clear as in the case of a strongly adsorbing electrolyte. A strongly adsorbing anion like Cl^- might increase the mobility of the atoms in the top layer [72], this can help to remove reconstruction.

Presently it is not well understood why the transition from the reconstructed to the unreconstructed surface is only gradual. It is possible that when the charge is removed from the surface in a weakly adsorbing electrolyte the unreconstructed surface cannot be more stable than the reconstructed surface. A theoretical study done recently [74] suggests that the energies of the reconstructed (1x2) and (1x3) structures are equivalent and more stable than the (1x1) unreconstructed structure without any applied potential on the surface [75].

Summary

This study shows there is a very weak potential dependence of the rotational anisotropy of the SHG signal from the Au (110) electrode in 0.01 M $HClO_4$. The data was well fitted with the modified C_s model with the extra three-fold component which shows that the overall symmetry of the surface is C_s. It was found that the second order nonlinear susceptibility for both the reconstructed (1x2)/(1x3) and unreconstructed (1x1) surface has a large three-fold symmetry component. The three-fold components are originating from the C_s symmetry and from the (111) microfacets. In conclusion, we suggest that the reconstruction of the Au (110) surface in a weakly adsorbing electrolyte is occuring gradually in the potential range studied.

References

[1] R.G. Lerner,G.L.Trigg editors; "*Encyclopedia of physics*" 2nd ed. (1990) VCH, N.Y.

[2] W. Moritz, D. Wolf; Surf.Sci. **88** (1979) L29.

[3] I.K. Robinson; Phys.Rev. Lett. **50** (1983) 1145.

[4] O.R. Melroy, M.G. Samant, G.L. Borges, J.G. Gordon, L. Blum, J.H. White,M.J. Albarelli, M. McMillan, H.D. Abruña; Langmuir **4** (1988) 728.

[5] M.G. Samant, M.F. Toney, G.L. Borges, J.G. Gordon, L. Blum, O.R. Melroy, J.Phys. Chem. **92** (1988) 220.

[6] B.M. Ocko, J. Wang, A. Davenport, H. Isaac; Phys. Rev.Lett. **65** (1990) 1466.

[7] J. Wang, A. Davenport, H. Isaac, B.M. Ocko; Science **255** (1991) 1416.

[8] X. Gao, A. Hamelin, M.J. Weaver; Phys.Rev. Lett. **67** (1991) 618.

[9] X. Gao, A. Hamelin, M.J. Weaver; J.Chem. Phys. **95** (1991) 6993.

[10] X. Gao, A. Hamelin, M.J. Weaver; Phys.Rev. B **44** (1991) 10983.
M.J. Weaver, X. Gao; Ann. Rev. Phys. Chem. **44** (1993) 459.

[11] P. N. Ross, J. Lipkowski editors; "*Structure of Electrified Interfaces*" (1993) VCH, New York, Chapter 2

[12] G.L. Richmond; Langmuir **2** (2) (1986) 132.

[13] V.L. Shannon, D.A. Koos, J.M. Robinson, G.L. Richmond; Chem.Phys. Lett. **142** (1987) 323.

[14] D.A. Koos, G.L. Richmond; J.Chem.Phys. **93** (1990) 869.

[15] D.J. Campbell, R.M. Corn; J.Phys.Chem. **92** (1988) 5796.

[16] Y.R. Shen; Nature **337** (1989) 519.

[17] P.N. Ross, J. Lipkowski; "*Adsorption of molecules at metal electrodes*" (1991). VCH, New York

[18] H.W.K. Tom et al.; Surf.Sci. **172** (1986) 466.

[19] A. Hamelin; In "*Modern Aspect of Electrochemistry*" edited by B.E. Conway, J.O'M. Bockris and R.E. White **16** (1985) 1, Plenum Press New. York.

[20] Edited by S. Parker; "*Solid State Physics Source Book*" (1987) McGaw Hill, New York

[21] C. Giacovazzo. editor; "*Fundamentals of Crystallography*" (1992) Oxford, Oxford

[22]a S. Strbac, R.R. Adzic, A. Hamelin; J.Electroanal.Chem. **249** (1988) 291.

[22]b A. Hamelin, J.Electroanal.Chem. **142** (1982) 299.

[23] A. Friedrich, B. Pettinger, D.M. Kolb, G. Lupke, R. Steinhoff,G. Marowski; ChemPhys.Lett. **163** (1989) 123.

[24]a A. Friedrich, C. Shannon, B. Pettinger; Surf.Sci. **251/252** (1991) 587.

[24]b D.A. Koos, V.L.Shannon, G.L. Richmond; Phys.Rev.**47** (1992) 4730.

[25] J.O'M. Bockris, S.U.M Khan; "*Surface Electrochemistry*" (1993) Plenum Press, New.York.

[26] D.M. Kolb, J. Schneider; J.Electrochimia Acta **31** (1986) 929.

[27] A.J. Bard, L.R. Faulkner; "*Electrochemical Methods*" (1980) Wiley, New York.

[28] A. Hamelin; J.Electroanal. Chem. **329** (1992) 247.

[29] H. Angerstein-Kozlowska, B.E. Conway, A. Hamelin, L. Stoicoviciu; Electrochim. Acta. **31** No.8 (1986) 1051.

[30] W. Schommers, P. von Plankenhagen eds.; "*Structure and Dynamics of Surfaces*" I - II. **41** (1986) and **43,** (1987) Springer, Heidelberg

[31] E. Tosatti, M. Bernasconi; Surface Science Reports, **17** (1993) 363.

[32] P.J. Estrup. In "*Chemistry and Physics of Solid Surfaces*" Vanselow R, Howe R. eds., Springler Series in Chemical Physics 35. Vol **V.** (1984) p:205.

[33] K.P. Bohnen, K.M. Ho; Electrochimia Acta **40** (1995) 129.

[34] P. Guyot-Sionnest, A. Tadjeddine;J.Chem.Phys. **92** (1990) 734.

[35] W. Moritz, D. Wolf; Surf.Sci. **163** (1985) L655.

[36] W. Moritz, D. Wolf; Surf.Sci. **234** (1990) L281.

[37] M.S. Zei, G. Lempfuhl, D.M. Kolb; Surf.Sci. **221** (1989) 23.

R. Michaelis, D.M. Kolb; Surf. Sci. Lett. **234** (1990) L281.

[38] B.M. Ocko, G. Helgesen, B. Schardt, J. Wang, A. Hamelin; Phys. Rev. Lett. **69** (1992) 3350.

[39] X. Gao, G.J. Edens, A. Hamelin, M.J. Weaver; Surf.Sci. **318** (1994) 1-20

[40] P.A. Franken, A.E. Hill, C.W. Peters, G. Weinreich; Phys.Rev.Lett.**14,** (1965) 973

[41] T. V. Higgins; *Laser Focus World* (1994) August, p:67

[42] M. Born, E. Wolf; "*Principles of Optics*" (1959) Pergamon Press,Oxford

[43] T. V. Higgins; *Laser Focus World* (1994) July, p: 91.

[44] A. Yariv; "*Quantum Electronics*" 3 rd edition (1989) Wiley New.York.

[45] J.E. Sipe, D.J. Moss, H.M. van Driel; Physical Review B **35** (1987) 1129

[46] R.J. Pressley editor.; "*Handbook of Lasers*" (1971) CRC Press, Cleveland, p:489

[47] B. Pettinger, J. Lipkowski, S. Mirwald, A. Friedrich; J. Electroanal. Chem. **329** (1992) 289

[48] Y.R. Shen;"*The principles of nonlinear optics*" (1984) Wiley New.York.

[49] N. Blombergen; "*Nonlinear Optics*" (1965) W.A. Benjamin Inc. New.York

[50] J. I. Steinfeld; "*Molecules and Radiation*" 3rd edition (1989) MIT Press,Cambridge, Mass.

[51]a T.M.J. Wijers, T. Rasing, R.W.J. Hollering; Solid State Comm. **85** (1993) 233

[51]b. A.Liebsch; Phys.Rev.Lett. **61** (1988) 1233

[52] A. C. Newel, J. V Moloney; "*Nonlinear Optics*" (1992) Adison-Wesley, New York

[53] F.J. Nye; "*Physical properties of crystals*"(1985) Clarendon Press, Oxford

[54] S. Bhagvantam; "*Crystal symmetry and Physical Properties*" (1966) Academic Press, London, New york

[55] D.M.Considine editor: "*Van Nostrand's Scientific Encyclopedia*" 6th edition(1983) by Van Nostrand Reinhold Company Inc.New.York.

[56] A.J.C. Wilson: "*X-ray Optics*" (1949) Methuen & Co.LTD, London

[57] A. Guinier: "*X-ray Diffraction*" (1963) W.H. Freeman and Company, New.York.

[58] S. Morin; "*Masters Thesis*" (1990) University of Guelph

[59] E. Wood; "*Crystal Orientation Manual*" (1963) Columbia Univ. Press, New York

[60] D. Dickertmann, F.D. Koppitz, J.W. Schultze; Electrochimia Acta **21** (1976) 967

[61] R. B. Ross;"*Handbook of metal treatment and testing*" (1977) E.& F.N.Spon, Wiley, London, New York

[62] W.J.M. Teggart; "*The electrolytic and chemical polishing in Industry and Research*" 2nd rev. ed. (1959) Pergamon Press, London

[63] J. Korita, J. Dvorak; "*Principles of electrochemistry*".(1987) Wiley,New York

[64] G. Shugar, A.J. Dean; "*The chemists ready reference handbook*". McGraw-Hill, New.York.

[65] A.J. Mabbott; J. Chem Ed. **60** No.9 (1983) 697

[66] O. Svelto, edited by D.C.Hanna; "*Principles of Lasers*" (1989) 3rd ed. Plenum,New York

[67] "*Active Mode-Locked Laser System Operating, Maintenance and Servicing manual*". *(1989)* Lumonics LTD, Rugby, Warwickshire, England

[68] B.E.A. Saleh, M.C. Teich; "*Fundamentals of photonics*" (1991) Wiley New.York.

[69] D.P. Woodruff, T.A. Delchar; "*Modern Techniques of surface science*" (1992) Cambridge, Cambridge.

[70] M.J. Weaver, X. Gao; Surf.Sci. **313** (1994) L775.

[71] O.M. Magnusen, J. Weichers, R.J. Behm; Surf.Sci. **289** (1993) 139.

[72] B. Pettinger, S,Mirwald, J. Lipkowski; Appl. Physics **60** (1995) 121.

[73] E.Vlieg, I.K. Robinson, K. Kern; Surf.Sci. **233** (1990) 248.

[74] T. Rasing, C.W. van Hasselt; Surf.Sci. **251/252** (1991) 467.

[75] C.D. Keefe, M. Dionne, E. Revesz, M. Morin; submitted to J. Electroanal. Chem. (1995) Nov.